AN ABSTRACT OF THE THESIS OF

Ramon K. Yoshiura for the degree of Master of Science in Nuclear Engineering presented on June 8, 2018.

Title: Heat Loss Characterization of NIST-1's Containment Vessel

Abstract approved: _____

Qiao Wu

NuScale Power has designed a small modular reactor using natural circulation cooling dependent systems for both steady-state and transient operations. The NuScale Integral Test System (NIST-1) facility was built to supply test data to NuScale Power to verify and validate computer codes for the NuScale Power Module (NPM) with the goal to satisfy the Nuclear Regulatory Commission's nuclear power plant certification criteria. The safety systems tested in NIST-1 heavily rely on the characterization of the heat transfer between the Containment Vessel (CNV) and Cooling Pool Vessel (CPV) via the Heat Transfer Plate (HTP) since the CNV acts as the cavity to contain steam leakage during an accident in the actual NPM. To ensure the heat loss in the CNV via insulation is small enough to be negligible and not affect test data, Computational Fluid Dynamics (CFD) program STAR CCM+ was used to simulate the test data from High Pressure Test (HP) 16b to analyze the heat loss. Grid convergence was achieved and results show good agreement with the HP-16b's test data concluding the CNV heat loss to be minimal and negligible.

Heat Loss Characterization of NIST-1's Containment Vessel

by

Ramon K. Yoshiura

A THESIS

submitted to

Oregon State University

in partial fulfillment of
the requirements for the
degree of

Master of Science

Presented June 8, 2018
Commencement June 2018

Master of Science thesis of Ramon K. Yoshiura presented on June 8, 2018.

APPROVED:

_____

Major Professor, representing Nuclear Engineering

_____

Head of the School of Nuclear Science and Engineering

_____

Dean of the Graduate School

I understand that my thesis will become part of the permanent collection of Oregon State University libraries. My signature below authorizes release of my thesis to any reader upon request.

_____

Ramon K. Yoshiura, Author

ACKNOWLEDGEMENTS

TABLE OF CONTENTS

TABLE OF CONTENTS (Continued)

TABLE OF CONTENTS (Continued)

LIST OF FIGURES

LIST OF FIGURES (Continued)

LIST OF FIGURES (Continued)

LIST OF TABLES

LIST OF ACRONYMS

HRT Human Upper Respiratory Tract. 12, 13

HTP Heat Transfer Plate. xii–xiv, 5, 7, 16, 24, 51, 54, 55, 58, 60, 61, 63, 66, 79, 83, 85, 86, 88, 89, 91, 96–98, 100–106

HX Heat Exchangers. 17–19

MASLWR Multi-Application Small Light Water Reactor. xi, 48, 49

NDA Nondisclosure Agreement. 48, 64, 77

NDSU North Dekota State University. 12, 13

NIST-1 NuScale Integral Test System. vii, viii, 1, 5, 7, 8, 16, 48–54, 60, 64, 66, 67, 100

NPM NuScale Power Module. 4, 5, 50–52

NPP NuScale Power Plant. 5

NRC Nuclear Regulatory Commission. 3, 5, 53

NS Navier Stokes. 43, 45–47

OSU Oregon State University. 1, 48, 49

PAFS Passive Auxiliary Feedwater System. x, 17

PASCAL PAFS Condensing Heat Removal Assessment Loop. 17

PWR Pressurized Water Reactor. 3–5, 14, 49

PZR Pressurizer. 4, 50

QSS Qausi-Steady State. 18, 19

NOMENCLATURE

α_i Phase Volume Fraction

$\bar{a}$ Time Averaged Undetermined Fluid Property

$\dot{m}_{ij}'''$ Mass Transfer Rate per Volume from one phase to another (kg/m³·s)

$\dot{m}_{ij}''$ Mass Transfer Rate per Area from one phase to another (kg/m²·s)

$\hat{i}$ x direction

$\hat{j}$ y direction

$\hat{k}$ z direction

μ Dynamic Viscosity (kg/m· s)

μ_i Phase Dynamic Viscosity (kg/m· s)

ρ Density (kg/m³)

ρ_i Phase Density (kg/m³)

σ_{lg} Interfacial tension between the liquid and low-density gas phase (N/m or kg/s²)

σ_{lv} Interfacial tension between the liquid and vapor phase (N/m or kg/s²)

σ_{sg} Interfacial tension between the solid and low-density gas phase (N/m or kg/s²)

σ_{sl} Interfacial tension between the solid and liquid phase (N/m or kg/s²)

σ_{sv} Interfacial tension between the solid and vapor phase (N/m or kg/s²)

τ Time Elapsed (s)

$\vec{F}$ External Forces (kg· m/s^2)

$\vec{g}$ Gravitational Acceleration in respect to some direction (m/s^2)

$\vec{q''}$ Angular Heat Flux (W/m^2)

$\vec{v}$ Velocity in some direction (m/s)

a Undetermined Fluid Property

a' Fluctuated Undetermined Fluid Property

$c_{p,i}$ Phase Specific Heat (kJ/kg·°C)

c_p Specific Heat (kJ/kg·°C)

D_i Molecular Diffusivity (m^2/s)

E Energy (J or kg·m^2/s^2)

e_a^{21} Approximate Relative Error

E_i Phase Energy (J or kg·m^2/s^2)

f_{bg} Background Molar Fraction

f_i Mole Fraction

GCI_{fine}^{21} Fine Grid Convergence Index

h Convective Heat Transfer Coefficient (W/m^2·K)

h_s Average Grid Size (m)

k Conductive Heat Transfer Coefficient (W/m·K)

N Total Number of Phases

n	Mole
N_c	Number of Cells
N_c	Number of primary phases under phase change
N_s	Number of secondary phases
P	Pressure (Pa or kg/m·s^2)
p	Order of Accuracy
P_i^*	Pure Vapor Pressure (Pa or kg/m·s^2)
P_i	Partial Vapor Pressure (Pa or kg/m·s^2)
q''	Heat Flux (W/m^2)
r	Grid Refinement Factor
S_α	Volume Source Term (kg/m^3·s)
S_h	Source Term (J or kg·m^2/s^2)
Sp_{ls}	Spreading Coefficient (N/m or kg/s^2)
T	Temperature (K)
t_0	Initial Time (s)
T_L	Liquid Temperature (K)
T_S	Surface Temperature (K)
T_V	Vapor Temperature (K)
u_i	Velocity in Direction i
V	Volume (m^3)

V_i Phase Volume (m^3)

W_{bg} Background Molar Weight (g/mol)

W_i Molar Weight (g/mol)

w_{sl} Work of Adhesion (N/m or kg/s^2)

x_i Length in Direction i

Y_i Mass Fraction

Chapter 1: Introduction

This thesis is to investigate the heat loss of the containment of the scaled down NuScale Small Module Reactor (SMR), the NuScale Integral System Testing (NIST-1) facility at Oregon State University (OSU) using Computational Flow Dynamics (CFD) data as an approximation with NIST-1 experimental test data.

In the engineering field, various designs are being imagined everyday and could potentially play important roles in society. But for every design there are degrees of uncertainty that cannot be determined at the stage of concept. In a normal but effective case would be the automobile. It has served society immensely and at the stage of concept there would have been oversights over oversights. Usually building a prototype or mockup and test running would help extract this kind of information. On the other hand, nuclear reactor designs take a different approach. Nuclear reactors are one of the most safest methods to produce electricity to the equivalent level of fossil fueled power plants. Before new designs are certified to be commercialized, the safety and functionality must be well investigated. For even building a prototype (extremely expensive and time consuming to build with multiple regulations to suffice), the safety features must be validated. Thus, shortcoming identification and test verification are unlikely (at least in the U.S.) to be conducted via prototype. The other alternative is to simulate the nuclear reactor using validated computer programs. Such codes are available and customizable. Although with computer programs, there are physics that still remain unknown and even with the known set of equations, there is not enough computational power to solve all variables. Accompanied with the unknown factor and computational difficulties, the associated uncertainties are unpredictable. To justify the uncertainty via actual data is required. Since actually building a prototype

would require safety feature and proof of concept which is why one build a prototype in the first place, building a down-scaled version of the original design using electrical heaters to substitute nuclear fuel rods to generate actual data is more realistic. The method to down-scale while preserving the physics as the original, is called scaling. With the actual data, both simulated and generated data can be cross-referenced to check the validity of the simulation. In the nuclear industry, this process is called validation. Figure 1.1 shows a simple scheme of how a design/code validation would work.
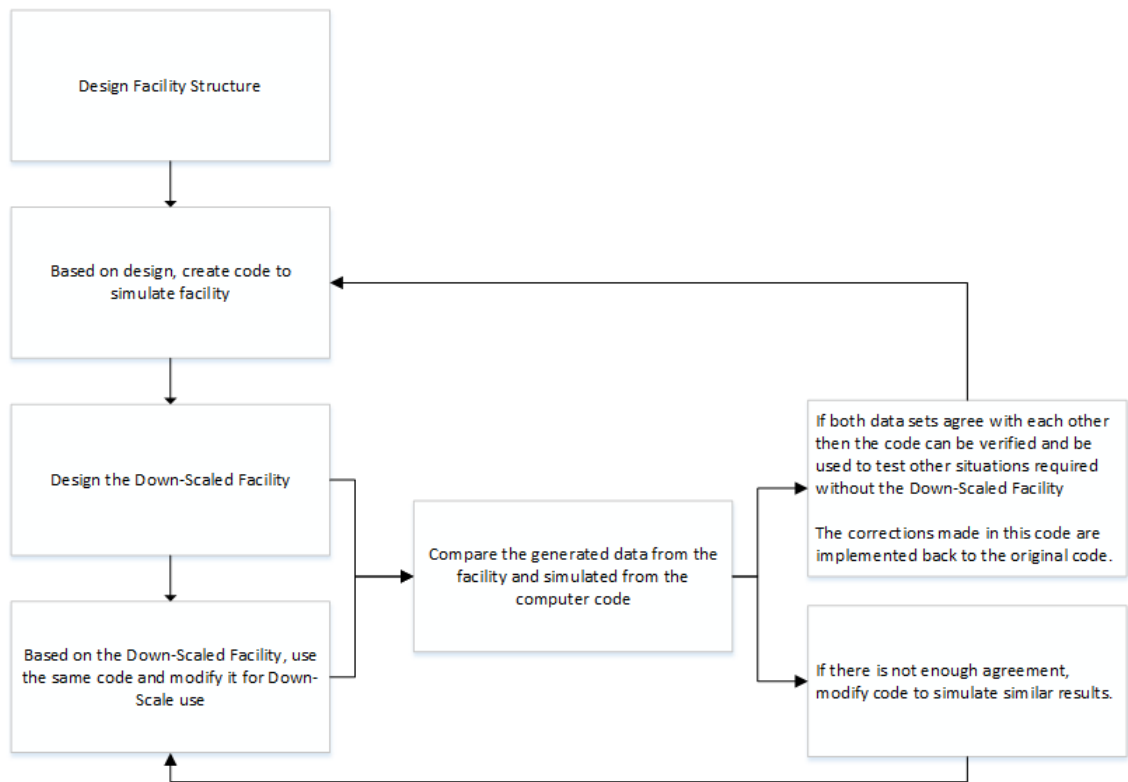
Figure 1.1: The general validation process.

Details concerning the background, motivations, and objecives are given in section 1.1, 1.2, and 1.4.

1.1 Background

In the nuclear power industry, completing the design is one thing but getting it approved and licensed in the United States government is another. The nuclear power industry is carefully regulated by the Nuclear Regulatory Commission (NRC). Under the NRC specific federal codes have been set to assure safe operation of the power plant and safety of the surrounding public. For new or semi-new designs, the NRC has placed provisions of Title 10 of the Code of Federal Regulations (CFR) Part 52 (10 CFR Part 52) "Licenses, Certifications, and Approvals for Nuclear Power Plants" to govern the issuance of standard design certifications, standard design approvals and other kinds of licenses [12]. Each design certification or power plant license is accompanied with detailed instructions of what applications must be completed. In the normal case, an issuance of the standard design certification would be the first to apply for. The application itself requires the following information: purpose of certification, financial information, general and specific descriptions of how the power plant functions (including subsystems as well), safety analysis, and other information that are pertinent to the NRC [13]. Although any party can submit their design to the NRC, the time required to review the application and willingness to approve may differ depending on the technology. Judging from the past of the NRC, a lot of time and effort has been spent to examine the validity and safety of the conventional design of the Pressurized Water Reactor (PWR) and Boiling Water Reactor (BWR) water reactors. Thus, submitting a standard design approval such as the AP-1000 from Westinghouse was relatively smooth. If the new power plant design was a molten salt reactor, it would be doubtful if the AP-1000 would be certified as it is today.

Today, NuScale Power has submitted their application for the standard design certification. The following figure shows the visual basic structure of the NuScale module and is provided by the NRC [1]:
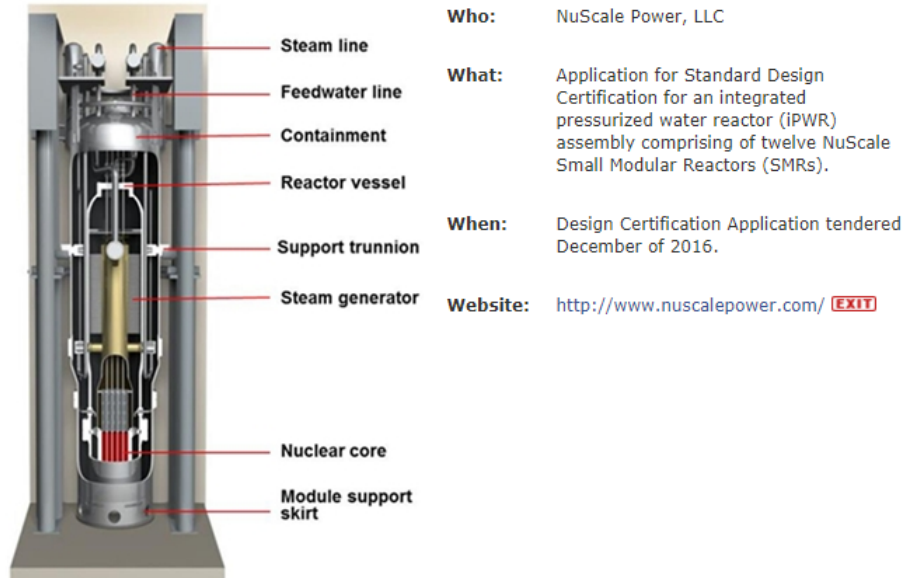
Figure 1.2: Basic structure of the NuScale module [1].

The NuScale Power Module (NPM) is a natural circulation cooling dependent system for both steady-state and transient operations. As the NPM being a PWR, basic components such as the reactor pressure vessel (RPV), Pressurizer (PZR), containment vessel (CNV) are in place. The NPM design RPV has an integrated PZR at the top with a baffle plate at the end of the PZR to separate the PZR and primary cooling flow. Opposed to typical PWR designs (reactor cooling pump transporting cooled primary water to RPV), the flow within the RPV is driven solely by natural circulation. The water heated by the core loses density and subsequently rises through the hot leg riser (also called a chimney) do to buoyancy forces. The rising water is redirected back down at the upper plenum crossing through helically coiled heat exchangers (acts as SG in secondary loop) cooling the primary water and increasing the water density which further accelerates downward flow. The lower plenum returns the water flow back to the core. The flow is thus driven by density change and geometry. The water in the heat exchanger vaporizes into superheated steam and sent to turbines. The RPV is in-housed in

the CNV where it is maintained as a vacuum during normal operations to restrict conduction and convection while the heat loss is minimized to thermal radiation. The NuScale Power Plant (NPP) has twelve units of this type of RPV in each individual cooling pool in a single given facility. The cooling acts as the ultimate heat sink. With all passive safety systems in place, the NPP is designed to operate safely in the event of an accident without emergency cooling pumps and off-site power.

Despite the NPM being a modified PWR, the Emergency Core Cooling Systems (ECCS) are there mainly to drive natural circulation and is not the conventional forced flow cooling systems. Combined with the innovative reactor small module setup, it is difficult for the NRC to be 100% confident and use previous PWR examination experience to apply to the NPM. For this reason NuScale Power must build an application with specific details on how the new concept will function and substantial data to support it.

As discussed earlier in section 1, down-scaling the design and generating data to validate the computer program to prove design concept is probably the most effective and relatively inexpensive. NuScale Power has acted on this method by building NIST-1. The details of the NIST-1 facility will be further explained in section 4. The data generated by the NIST-1 facility is used to validate the computer program that simulates the actual power plant design.

1.2   Motivation

In any test facility with heating involved, insulation around the pipes and walls are standard to establish adiabatic conditions and to minimize the loss of heat. For the NIST-1 facility's case, characterizing the heat transfer between the CNV and the Cooling Pool Vessel (Cooling Pool Vessel (CPV)) via the Heat Transfer Plate (HTP) is paramount (CNV, CPV, and HTP functions will be explained in section

4). To be clear of what the CNV and CPV represent on the actual NuScale Power module, from Figure 1.2 the CNV is named the same and the CPV is the space open in between the CNV and the remained outer-space which is normally filled with water as a heat sink. In order to correctly measure how much heat has entered and left the CNV, proper insulation is required. With insulation installed, it is standard to make boundary conditions on the outer wall to be adiabatic. To ensure the heat loss to the insulation (eventually to the ambient air) is minimal enough to be negligible, it is the duty of this masters thesis to investigate this matter using STAR CCM+. By simulating a test that already has been conducted, the amount of heat loss will be assessed and will be validated by using test data from that exact test.

1.3 Remarks

The NIST-1 experiment that will be further described in section 5, consists of injecting superheated steam into the CNV. This process encompasses the injection method, characterization of turbulence, condensation on CNV wall, pressure build up, and heat transfer of all kinds including convection and conduction. Through proper analysis, each aspect would have to be validated in the CFD simulation to project the correct wall temperature distribution of the CNV, insulation, HTP, and eventually the heat leaving the system to the ambient air. To realistically complete all tasks within the Masters thesis level, it would be vastly cumbersome. Although months of effort was made to tackle all aspects, it was determined by the author that it would be improbable to realize (specific details on what portions were limiting are in section 6) and the simulation was solely conducted with CNV, HTP, and insulation structures with boundary conditions concerning the known CNV wall temperatures. If the fluid region were added, the simulation would be no longer an approximation but a validation processes in CFD terms.

Regardless of what was excluded from the simulation, the literature review and theory sections in this thesis include all fields that are related to the full simulation with fluid regions. It is the intent of the author to provide this thesis not only as an opportunity to publish research results but also to educate readers with no background in thermal hydraulics. Combined with the literature review and theory, the physics governing NIST-1's experiment and reasons given for why such decisions were made will hopefully be more understandable and clear.

1.4   Thesis Objective and Overview

While this thesis is to investigate the heat loss in NIST-1's CNV, the following are the objectives to thesis:

- Successfully build CNV and HTP geometry.

- Determining and importing required test data for boundary conditions and comparison.

- CFD physical model determination.

- Successfully run simulations for various spatial and temporal grids to achieve grid convergence.

- Compare test and simulated, and analyze the simulated heat flux for valid heat loss determination.

The composition of this thesis is divided into eight parts: introduction, literature review, NIST-1, theory, experiment, simulation, results, and conclusion. The following list will summarize each chapter to provide the reader with a clear view of what to expect:

- Chapter 1 - Introduction: A detailed description of how recent nuclear power plants are licensed, how a nuclear power plant concept can be proved, and the main motivation of simulating the CNV of NIST-1.

- Chapter 2 - Literature Review: A review of old to recent relevant topics centered on scaling, computational fluid dynamics, condensation, film flow, and heat loss in containments.

- Chapter 3 - NIST-1: A basic description of how the relevant components function.

- Chapter 4 - Theory: A description of the governing concepts and equations.

- Chapter 5 - Experiment: Specifics on the experiment that was simulated by STAR CCM+.

- Chapter 6 - Simulation: Details on the simulation settings including initial and boundary conditions.

- Chapter 7 - Results: Representation of the simulated data with comparison of the facility generated data.

- Chapter 8 - Conclusion: Statements of the agreement between the generated and simulated data and final analysis on the heat loss to the surroundings.

Chapter 2: Survey of Literature

Before introducing the content of the literature survey, it must be noted that condensation and film flow/Droplet flow were initially part of the phenomena to simulate in STAR CCM+. For reasons that will be explained in section 6, both phenomena were excluded from the simulation and the two phase flow problem was changed to a convection/conduction heat transfer problem. Regardless of this change, condensation and Film Flow/Droplet Flow will be part of the literature survey.

The following fields have been chosen to keep the reader informed of recent efforts made in fields that are relevant to this thesis:

- STAR CCM+: The main tool used to simulate heat loss.

- Heat Transfer CFD: The analysis mode used for the simulation.

- Two-Phase CFD: The main drive of heat transfer.

- Condensation: The main mode of phase change.

- Film Flow/Droplet Flow: Possible flow on walls.

- Insulation: Showing developments in insulation.

2.1   STAR CCM+ and CFD in General

STAR CCM+ is a commercial multidisciplinary engineering simulation software that covers stress analysis to multiphase flow. Given the correct physics models and boundary conditions, it delivers accurate and efficient simulations [14]. The

simulation method taken is called CFD. Fundamentally, the equations to be solved are either Lagrangian or Eularian. The continuity, momentum, and energy equation are simultaneous solved by replacing the continuous problem domain with a discrete domain grid (also called discretization) [15]. Examples of methods of discretization would be the finite difference method and the finite volume method. For the simulation that will be introduced in section 6, a transient solution would not only be discretized spatially but in time as well. As described in section 1.1, CFD programs such as STAR CCM+ can build solutions for experiments that may cost more than the researcher is willing to pay. As examples of the STAR CCM+ appliance to the real world, the following list are actual simulations that were conducted on STAR CCM+ (information publicly provided by CD-adapco) [16]:

- **Solid Mechanics:** Fluid structure interaction on a ship's propeller

- **Reacting Flows:** Mass fraction of Carbon Monoxide in a glass furnace simulation

- **Rheology:** Multiple extrudate cases with various die cross sections

- **Multiphase Flow:** Lagrangian multiphase and film interaction for water management of a motorcycle

- **Acoustics:** Landing gear aeroacoustics

- **Heat Transfer:** Evaporator exiting from brazing furnace

Given the users skill and comprehension of CFD, STAR CCM+ is extremely capable and efficient.

2.2   Heat Transfer Computational Fluid Dynamics

There are three modes of heat transfer: conduction, convection, and radiation. The heat transfer portion of the code is solved with the energy equation. Now depending on the medium of the heat transfer, the mode of heat transfer can be determined. In CFD, as long as the type of initial or boundary condition is set to a temperature or heat flux (can be volumetric), the problem is then turned into a heat transfer problem. In the most simplest form, a solid material with insulated and heated surfaces would only require the energy equation (continuity and momentum are used but all equal to 0 due to no movement).

A more complicated form would be to integrate phase change and chemical reactions which add or remove heat from the system. In most cases, a full heat transfer simulation would encompass both simple and complicated modes. For example, analyzing the effectiveness of heat pipes in buildings with glazed facades can be categorized as a multi-material single phase problem or if the heated pipes are hot enough a multi-material two-phase problem [2]. With the doubled sided facade and cold/hot air temperature difference, single phase air heat transfer is easily simulated. From the Civil Engineering and Building Services of Technical University of Iasi, to test the efficiency of the heated pipes installed in glazed facades, the thickness of glass layers and cavity facade were held as variables to simulate. By using ANSYS, the quality and quantity of thermal heat flux for various temperature boundaries [2]. Comparing different cases, Figures 2.1 and 2.2 illustrates the capabilities of how heat transfer CFD can help the human society.
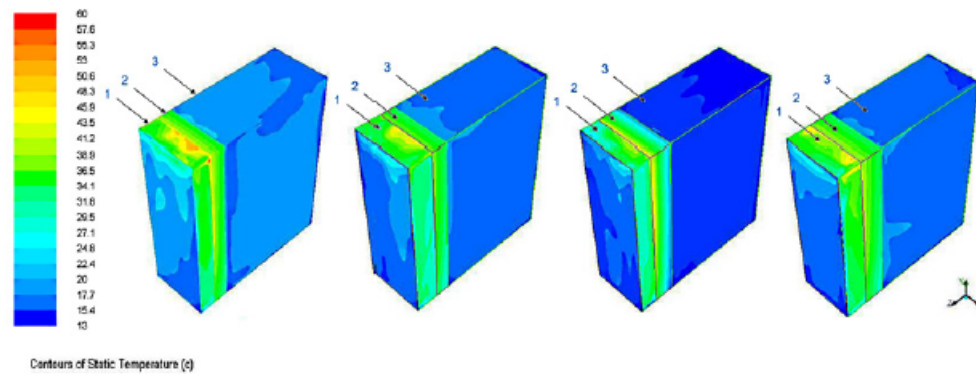
Figure 2.1: Contours of static temperature for all 4 cases [°C] [2]
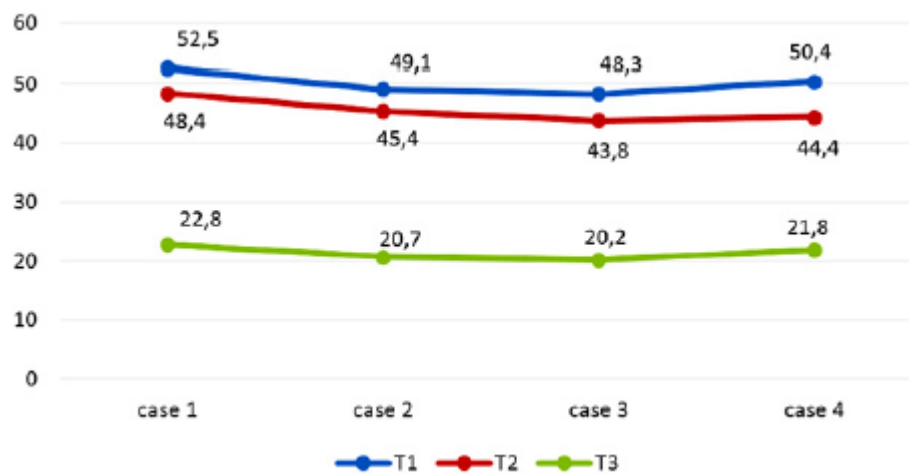
Figure 2.2: Mean temperature for all 4 cases [°C] T1 - temperature of cavity facade [°C];T2 - Temperature of autoclaved aerated concrete Wall[°C];T3 - Temperature of Room [°C] [2]

Another example of real world heat transfer CFD would be simulating certain functions of the human body. The Department of Industrial and Manufacturing Engineering of North Dekota State University (NDSU) has developed a heat transfer CFD simulation dealing with the Human Upper Respiratory Tract (HRT). To

assess extent of injuries in the HRT (caused by inhalation of hot or combustible gasses), NDSU has created a model that will display the temperature distribution of portions of the HRT which encompasses the nasal cavity, oral cavity, nasopharynx, oropharynx, trachea and the bronchi. By using the 3D geometry of the HRT based from MRI scans and computing via ANSYS, the temperature distribution was obtained and it was concluded that the highest temperatures existed around the nasal or oral cavity and the temperature decreased as going further deep into the HRT [3]. The visual result of the temperature distribution is shown in Figure 2.3.
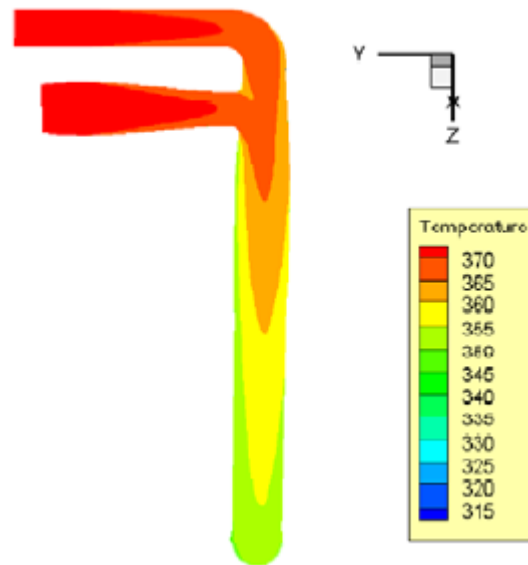
Figure 2.3: A cross-sectional temperature variation view (K) [3]

2.3 Two-Phase Flow Computational Fluid Dynamics

Two-phase flow can be categorized into two groups: single material two-phase flow and multi-material two-phase flow. Single material two-phase flow can only exist when phase change occurs or two phases of the same material are forcedly merged

in the same volume. However eventually, at some point phase change will occur. When looking at a two-phase flow problem using the mixture model, the physical interaction between the two phases makes the solution of conservation laws complex. Terms such as void fraction and flow velocity of each phase cannot be tracked at the same time. Flow models such as the slip ratio and the drift flux model are good examples of providing closure relations to enable conservation laws to be solvable. Combined with the flow model and closure relations, two-phase flow CFD is made possible. Examples of successful two-phase flow phase change simulations is abundant in not only in the nuclear industry, but in other engineering fields as well. The success of two-phase flow simulations is a major product of excellent code validation processes. Reverting to section 1, the importance of code validation is justified. To reveal how this two-phase validation process takes place, the content below will provide a relevant CFD program example.

As already discussed in section 2.1, STAR CCM+ is one of the CFD programs used commercially. Also in previous sections, ANSYS has been mentioned in multiple referenced sources. The example selected to represent two-phase validation is a code specialized in thermal-hydrualics and it is called 'NEPTUNE CFD', a French CFD program co-developed by Electricité de France and Commissariat á ÍEnergie Atomique with the goal to invent a new software platform for advanced two-phase flow thermal hydraulics simulations for developing next generation nuclear reactor simulation tools [17]. NEPTUNE CFD was used in a joint research project between French, German, and Spanish scholars to validate the two-phase flow models using open source experimental data produced by the Organisation for Economic Co-Operation and Development for BFBT and PWR Subchannel Bundle Test. The goal was to validate by comparing the void fraction at different distances from the heated wall. Starting with mesh sensitivity analysis to seek the optimized mesh size, finding the suitable bubble size to add to the simulation is important to calculate the correct void fraction. With all decisions finalized,

simulated and experimental void fractions were put in contrast. Figure 2.4 shows void fractions for three different locations at certain times.
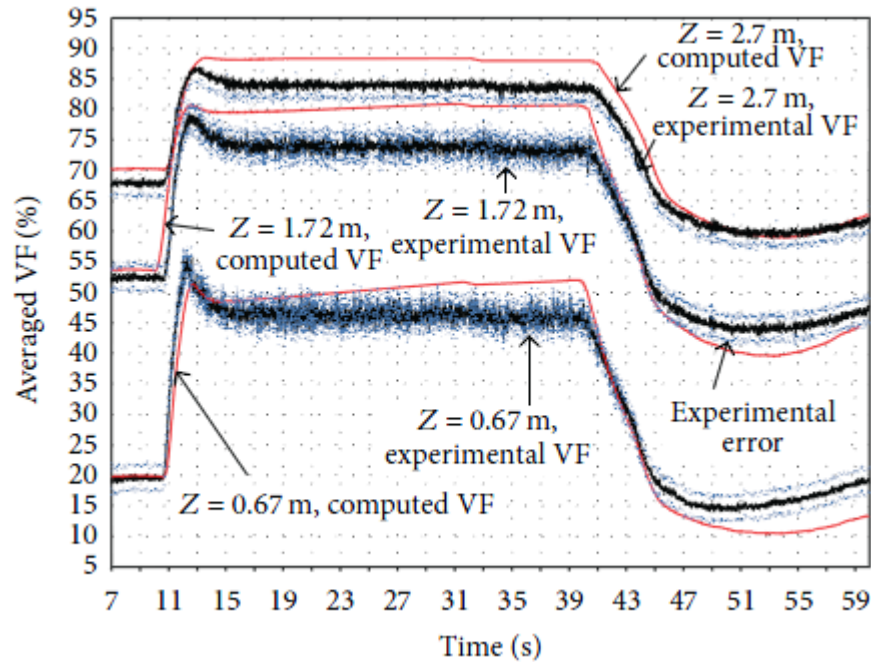
Figure 2.4: Comparison of the BFBT void fraction data and its measurement error ($\pm$ 2%) with the void fraction predicted by NEPTUNE CFD at three axial levels during the recirculation pump trip experiment [4]

It can be observed that the simulated results follows the trend of the experimental results but encloses relative errors as high as $\pm 30\%$. Although 30% may be insinuated as large deviations, correlations for two-phase flow and phase change are normally around the same magnitude. Considering the relative error being comparable to industry standards and the similarity in trends, the quality of the validation more than acceptable.

Added with the content above, Two-Phase flow CFD also includes turbulent model

validation which is still a completely complex field by itself. Two-Phase flow CFD is still developing but shows great potential.

2.4   Condensation

Condensation is the phenomenon that describes the phase change from vapor to liquid. More generally, phase change occurs when the phase change interface is established and latent heat is removed or added. On the stipulation that the phase change interface must exist before any phase transition can be made, phase change is a surface phenomenon. Removing and adding latent heat can be considered the act of releasing and absorbing thermal energy to a point where the threshold energy has either reached or lost to allow the molecular structure of some substance to change. In the microscopic scale, the energy within the molecule is the kinetic energy of atoms moving to a certain degree of freedom depending on the phase of the molecule (different phases correspond to different molecular density). Further discussion on the theory and equations of condensation will be mentioned in section 3.2.

Other than applications for condensation like distillation or rectification, the main aspect concentrated in thesis is the cooling heat transfer during phase change. In order to remove heat from superheated vapor, one way is to mix it with relatively cool fluids which is extremely invasive especially when it is mixed with heterogeneous fluids. Another but noninvasive method is to have cooled walls to remove enough heat to trigger phase change and further remove heat via condensation. At this point, the coldest temperature in the fluid is near the wall at the solid-fluid interface and a liquid droplet embryo is formed which may remain as a droplet or combine to become a film [9]. Such noninvasive vapor cooling mechanisms are referred to as passive cooling and has been recently added to post-Fukushima-Daiichi nuclear power designs. The CNV and HTP in the NIST-1 test facility simulates this exact phenomenon.

One example of other similar test facilities experimenting on condensation is the PAFS Condensing Heat Removal Assessment Loop (PASCAL) facility in Korea [5]. The objective of PASCAL was to validate the cooling performance of the PAFS system in the Advanced Power Reactor Plus (APR+) by using PASCAL as the scaled test facility. The PASCAL consists of a SG, steam supply line, Heat Exchangers (HX), Cold Tank (CT), and return water line. The heat exchanger exist within the cooling tank and while heat from the steam line is dissipated to the pool tank, the steam is being condensed via heat exchangers and the liquid water is sent back to the SG. Figure 2.5 shows the PASCAL facility as a whole.
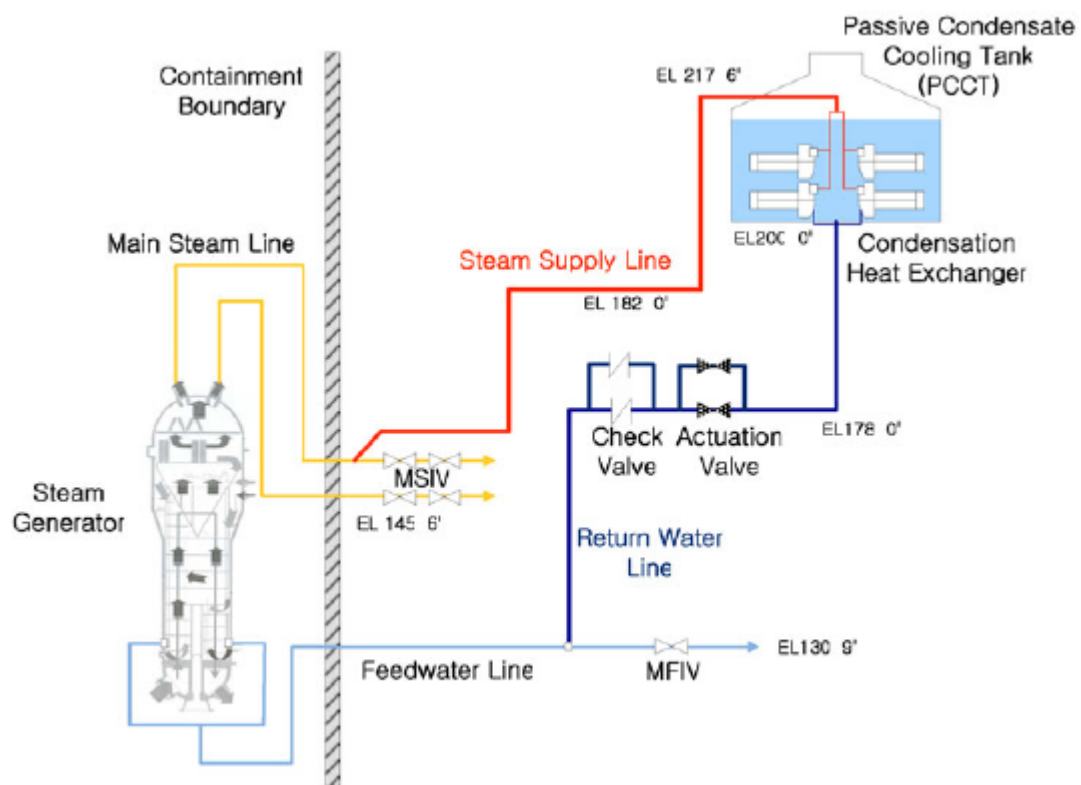
Figure 2.5: Schematic diagram of APR+ PAFS [5]

By conducting several tests setting the SG's heater power ranging from 300 kW to 750 kW, the Qausi-Steady State (QSS) of steam generation between steam condensation was achieved. Figures 2.6 and 2.7 shows the heat removal and flow rate from the SG and condensation HX.
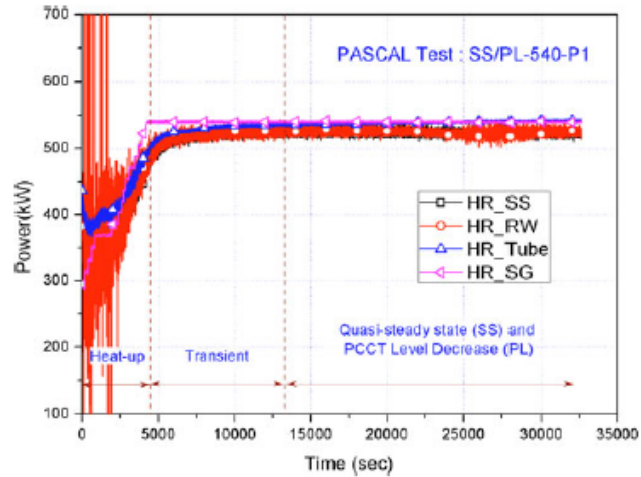
Figure 2.6: Heat removal rate [5]
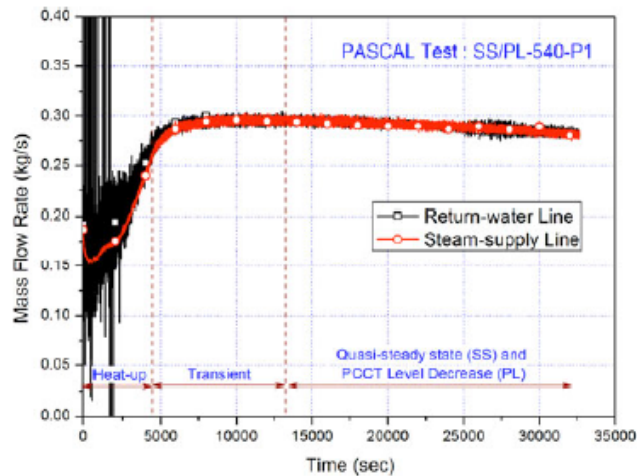
Figure 2.7: SG system flow rate [5]

Despite the main goal of the QSS testing was to measure the decrease of water level of the CT (HXs are located within the CT and heat emitted from the HX is large enough to wall boil), it proves the degree of condensation provided with passive methods was sufficient enough to maintain QSS, to supply water back to the SG, and released ample amount of latent heat to cause wall boiling.

For condensation modeling, correlations and simulated versions exist. In terms of correlations, methods such as Uchida's correlation and Dehbi's correlation are popular but leave out terms like pressure or do not take geometry into consideration. It is for this reason that numerical simulations must be implemented. Although numerical simulations done by programs (for example MATLAB or Python) can use discretized geometry and apply condensation models like lattice Boltzmann methods [18] to solve iteratively, only simple geometries can be simulated and even it is possible to model complex geometries, it would take a considerable long time and grand effort to realize. To apply complex geometries it is usually recommended to use CFD programs to care of geometric and meshing modeling. The only downfall to utilizing CFD programs is that the physical models provided may not characterize condensation as desired. An example of successful condensation CFD is a simulation done in Korea by the Department of Nuclear and Quantum Engineering of Korea Advanced Institute of Science and Technology where they used FLUENT to simulate external pipe condensation and validated it with the actual experiment setup data giving only 7% error [19]. Fortunately, FLUENT had the option for condensation modeling.

2.5   Film/Droplet Flow and Heat Transfer Properties

After condensation is induced on a solid wall, depending on the wetting surface the either dropwise or film condensation can take place. For dropwise condensation to be prevalent, the solid surface has to a poor wetted surface to limit the wetted area and to form a droplet.
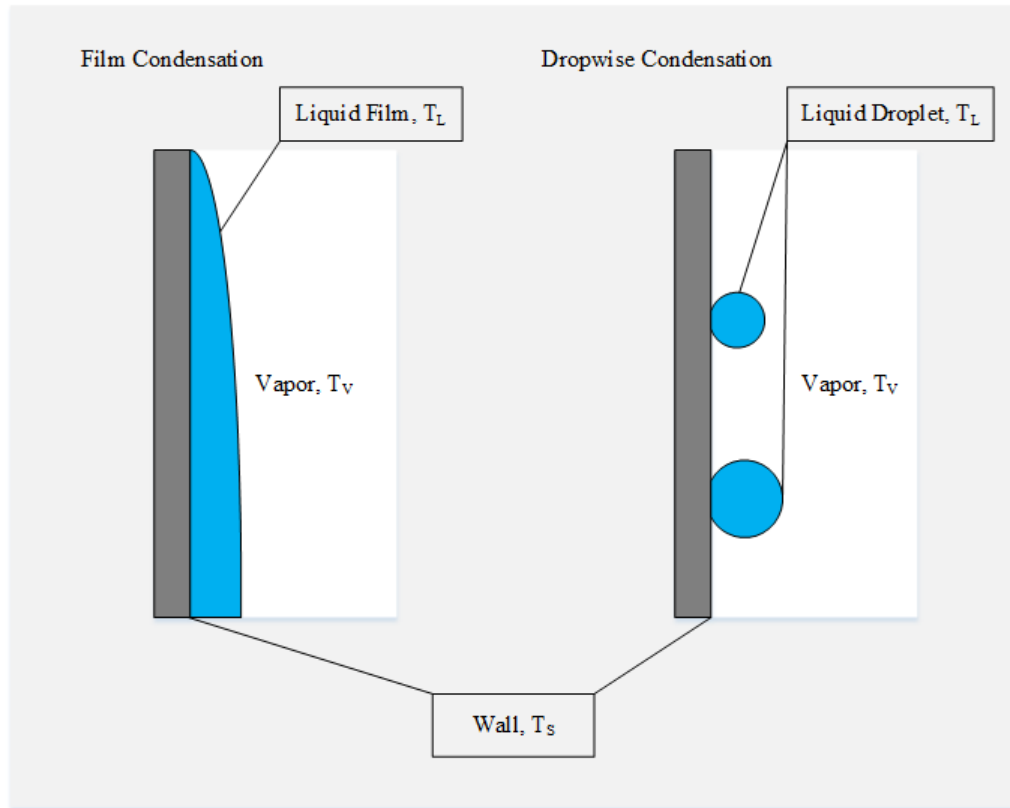
Figure 2.8: Types of Condensation. T_S is the surface temperature, T_L is the condensation temperature, and T_V is the vapor temperature.

From figure 2.8, it can be seen that film condensation covers the wall entirely creating a liquid interface between the vapor and the wall. The heat transfer between the vapor and wall will then be two stepped where the direction of heat transfer will be from the vapor to the film (convection) and the film to the wall (convection and conduction). Considering the wall temperature to be the coldest in the system, to promote enhanced condensation it would be best for the vapor to be directly in contact with the wall. With this in mind, dropwise condensation is the more effective mode since as the liquid droplets move, it provides more surface area on the wall to be exposed to vapor. Whether either modes are desired

or not would depend on the users intent (Typically in the order of $T_S < T_L < T_V$).

In research, depending on the objective of the experiment one could use hydrophobic (poor-wetting) and hydrophilic (well-wetting) surfaces to enhance certain characteristics of the flow or heat transfer. Besides choosing a more desired liquid to enhance intended properties, one may plate, code, or manufacture nano-structures onto the surface. A familiar application of coding for hydrophobic effects would be water repellent for vehicle windows. For one research group, nano-structures were used to create super-hydrophobic surfaces to enhance accelerated condensation rates [20]. By fabricating silicon nanopillars onto the surface, the wetted area on the surface was decreased and bubbles were suspended spontaneously from the surface once they grew to a certain size due to the excess of surface energy (surface energy will be further explained in section 3.3). Interestingly enough, the same nano-structure super-hydrophobic studies has also been applied to increase boiling properties as well at Drexel University Philadelphia. According to their research, nano-structures has increased the thermal conductivity by a factor of 2.6 compared to the same surface without special treatment [21].

For CFD simulations, depending on which physical models are chosen only specific condensation modes can be simulated. To the user these various options will determine flow and heat transfer of the fluids. It is for this reason that the user must absolutely know what kind of condensation is exhibited to produce valid simulations.

2.6   Insulation

Thermal insulation is in almost all manufacturing and engineering fields to prevent thermal energy from leaving the system. Typical insulation materials are foams, fibers, glass, vacuums, gasses, concrete and etc. More recently, composites, gels, multilayer insulations are being tested as well to accommodate for different situ-

ations. Such accommodations can be to minimize heat transfer efficiently while maximizing light transmittance. For such properties, the Dalian Polytechnic University's answer was to use a composite aerogel made out of SiO_2 and $Cs_{0.32}WO_3$ [22]. The SiO_2 is transparent, has good insulation properties and combined with $Cs_{0.32}WO_3$ will block infrared light as well. Another special accommodation would be insulation for vehicles experiencing high degrees of velocity. A combined research group between China and Sweden had the innovative idea to use multilayer insulation using fibrous (conductive) and gold-coated foils (radiative) to block extreme temperatures (hot and cold) while withstanding mechanical stress [23]. By using verified codes, the optimal number of layers for maximized effect was determined. The fact remains that for any kind of material, the increase in temperature will in some extent change material properties in such a manner that the conductive heat transfer coefficient will increase allowing more heat to be transferred.

2.7   Remarks

To matters clear, as mentioned in section 1.3 and at the beginning of section 2, the fluid region of the simulation was excluded for reasons noted in section 6. The simulation then becomes a part convection from ambient air and mostly conduction problem instead. Altough the content in this chapter includes many fluid physics, it is mainly here to educate readers with no background in thermal hydraulics and comprehend the thought process of why the fluid region was excluded.

Chapter 3: Theory

As noted in section 2, this thesis was originally intended to include two-phase flow and condensation. For this sole reason, the governing equations will encompass two-phase flow. This section will start from principle laws Conservation of Mass (COm), Conservation of Momentum (COM), and Conservation of Energy (COE) and then add equations from the STAR CCM+ manual for the applied physical models. For reasons that will be noted in section 6.4, the following models were chosen to simulate two-phase flow and solid heat transfer.

Fluid Physical Model:

Main Physical Model	Sub Physical model
Three Dimensional	N/A
Gradient	N/A
Implicit Unsteady	N/A
Gravity	N/A
Eulerian Multiphase (EM)	Multi-Component Gas Multi-Component Liquid
Volume of Fluid (VOF)	N/A
Multiphase Interaction	Multiphase Material Evaporation/Condensation VOF Phase Interaction
Segregated Flow	N/A
Reynolds-Averaged Navier-Stokes	N/A
K-Epsilon Turbulence	Realizable K-Epsilon Turbulence

Table 3.1: The physical models chosen in STAR CCM+ for the fluid volume

Solid Physical Model:

Main Physical Model	Sub Physical model
Three Dimensional	N/A
Gradients	N/A
Implicit Unsteady	N/A
Solid	N/A
Constant Density	N/A
Segregated Solid Energy	N/A

Table 3.2: The physical models chosen in STAR CCM+ for the solid volume

3.1   Governing Equations

Before proceeding into equations, all nomenclatures are provided in the beginning of the document and operators are shown in section A. When identifying the situation in question, the problem must be divided into two sections: solids and fluids (also known as liquid and gas). For the solid portion, it would include the CNV wall, HTP, and insulation. On the other hand, the fluid portion would be the initial CNV internal volume, the injected steam, and the condensate. The following subsections will describe the governing equations for the solid and fluid states:

3.1.1   Solids

The solids are on a macroscopic scale, stable, immobile, and most importantly does not deform under until a certain level of stress is applied. In the case of this paper, the solid is the CNV wall, HTP, and insulation. In reality due to heat expansion in the structure, the geometry may have some velocity due to deformation but very near zero. Despite the fact that heat expansion would suggest density change, the

change in time is assumed to be minimal and thus negligible.

With these assumptions, there should not be equations for COm since either side of the equation would only amount to zero. For COM, it becomes slightly more complicated. The advective forces can be ignored since it was already noted previously that any movement in structure was negligible. What forces are left would be the pressure balance between the atmospheric pressure and the CNV internal pressure. Due to steam injection, the internal pressure will accumulate while the atmospheric pressure will remain close to constant. This imbalance in pressure adds to the structure stress and may have a combination of plastic and elastic strain (meaning any deformations made by adding stress may or may not return exactly back to the original form before the stress had been added). Regardless of these possible force imbalance in structure, it can be observed from Table 3.2 that body stress models are not included. The final objective of this research is to determine the heat loss in the insulation and not to test the rigidness of the CNV. Another more practical reason for not adding stress models is not to further allocate computational power to unnecessary calculations.

Now that the mass and force equations has been excluded, what is left is the COE. The modes of heat transfer that do exists is typically convection and conduction. Heat radiation however is excluded since the fluid volume within the CNV is hotter than the CNV walls and the emissivity of insulation to the ambient surroundings is ignored. Since convection is between a solid and fluid, two locations will have this mode: outside the insulation and the inner walls of the CNV. Conduction exists in the CNV wall and in the insulation. Figure 3.1 provides the visual demonstration of where the different heat transfer modes are.
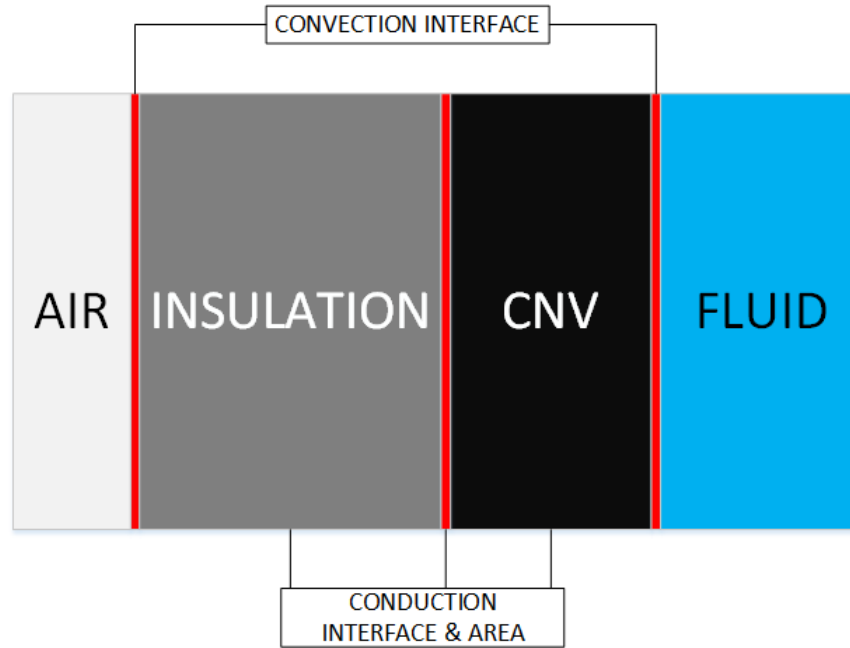
Figure 3.1: Diagram of convection and conduction locations

When setting the control volume from the inner CNV wall to the outside of the insulation, the COE is the energy balance between the convection from the fluid and ambient air. For the insulation and CNV, it would be the balance between convection and conduction. The following equations are expressions of convection and conduction in mathematical form:

Conduction: Fourier's Law

$$\vec{q''} = -k\nabla T \tag{3.1}$$

Conductive heat transfer can be defined as the thermal energy traveling within the same volume. When seen in the microscopic scale, vibrations (in gas and fluid kinetic energy) of the particle are inherited to particles with smaller vibrations. Conduction heat transfer coefficient k is a term that may vary by location and temperature. The spatial variance can be isotropic (same for any point), anisotropic

(direction dependent), homogeneous (same material), and heterogeneous (different material but same object with no contact resistance) [24]. For thermal variance, depending on the temperature of the substance in question, k may increase or decrease since the spacing between particles could vary. Thus when setting the value of k, it is essential to set the appropriate value for the given situation to correctly identify the amount of heat transfer. In Eq. 3.1, the temperature has a gradient for space. In cartesian coordinates, the gradient of temperature in space would then be the following:

$$\nabla T = \frac{\partial T}{\partial x}\hat{i} + \frac{\partial T}{\partial y}\hat{j} + \frac{\partial T}{\partial z}\hat{k} \tag{3.2}$$

Where Eq. 3.1 is the infinite medium heat transfer at one direction.

Convection: Newton's Cooling Law

$$q'' = h\left(T_S - T_L\right) \tag{3.3}$$

Convection heat transfer between a solid and liquid is a relation that takes viscous forces as the main method of energy transfer. Assuming there is no slip on the surface of the wall (fluid remains stagnant at wall coordinates), fluid particles attempting to go over the no slip boundary eventually approach free stream properties when the particles are above the viscous boundary layer [24]. This viscous boundary then triggers the thermal boundary layer to develop. Through experiments conducted by Newton, the rate of heat transfer via thermal boundary layer is proportional to the difference in temperature which yields Eq. 3.3. The convective heat transfer coefficient h can be a complicated task since it is highly dependent on what kind of fluid flow is present. There are numerous theories and correlations that have been developed to attempt to validly characterize h. To show how much h can vary, Table 3.3 has been provided from *Convection Heat Transfer* written by S. Kakac et al.

Fluid	Free Convection	Forced Convection
Gases	5-30	30-300
Water	30-300	300-10,000
Viscous	5-100	30-3,000
Liquid Metals	50-500	500-20,000
Boiling Water	2,000-20,000	3,000-100,000
Condensing Water Vapor	3,000-30,000	3,000-200,000

Table 3.3: Approximate Values of the Heat Transfer Coefficient h, $W/(m^2K)$

Given the experiment overview in section 5, the internal flow of the CNV is potentially film or dropwise flow. For theories and correlations concerning this field will be provided in section 3.3.

3.1.2   Fluid

From experiment overview in section 5, the fluid region of the test in question is single-phase flow at (t=0s) and afterwards immediately two-phase flow with non-condensable gas. Since sections 3.3 and 3.4 will discuss further details in condensation, the two-phase aspect of fluid flow for the VOF model will be represented in this section. For multiphase equations, the first decision that must be made is whether to solve the problem using Lagrangian or Eulerian equations. Lagrangian equations follows a particle as it moves in space and time. The key to using Lagrangian models in CFD is to determine how many particles is enough to correctly simulate the flow. However when dealing with large volumes, the required number of tracking particles becomes much too computationally expensive on the university level. Rather than tracking the particles, it is easier to set a control volume and solve each small portion which is also known as Eulerian methods. From Table 3.1, the final choice made was to use EM and VOF to solve through the fluid domain. The VOF model is capable of simulating immiscible fluid flows for different

phases where minimal total contact area between phases exist [8]. From section 5, steam is injected from the top of the CNV and condensation on the walls descend to the bottom thus producing a condensate pool. Since the steam is injected far away from the condensate pool, the phase interface area is minimal and suitable for the VOF model. The Eulerian Multiphase Mixture Model was another possible choice but was discarded due to having non-condensable gas in the actual test.

In detail, VOF is more tracking the interfaces between the phases. By sharing physical properties such as density, dynamic viscosity, and specific heat, solving one set of momentum and energy equation is only required. The following is how the physical properties are shared (CAUTION: the following equations are given in the STAR CCM+ manual [8]):

$$\rho = \sum_i \rho_i \alpha_i \tag{3.4}$$

$$\mu = \sum_i \mu_i \alpha_i \tag{3.5}$$

$$c_p = \sum_i \frac{c_{p,i}\rho_i}{\rho}\alpha_i \tag{3.6}$$

Where the volume fraction is defined as:

$$\alpha_i = \frac{V_i}{V} \tag{3.7}$$

Both momentum and energy balance equations are then the following:
<u>Momentum:</u>

$$\frac{\partial}{\partial t}\left(\rho\vec{v}\right) + \nabla \cdot \left(\rho\vec{v}\vec{v}\right) = -\nabla P + \nabla\left[\mu\left(\nabla\vec{v} + \nabla\vec{v}^T\right)\right] + \rho\vec{g} + \vec{F} \tag{3.8}$$

The relation between $\nabla\vec{v}$ and $\nabla\vec{v}^T$ in stress tensor terms is $\frac{\partial u_i}{\partial x_j}$ and $\frac{\partial u_i}{\partial x_j}$ where $\nabla\vec{v} = \frac{\partial u_i}{\partial x_j}$ is the spatial derivative in the j direction for i direction velocity u and

$\nabla \vec{v}^T = \frac{\partial u_j}{\partial x_i}$ is the spatial derivative in the i direction for j direction velocity u. $\vec{F}$ represents the external forces.

Energy:

$$\frac{\partial}{\partial t}(\rho E) + \nabla \cdot (\vec{v}(\rho E + P)) = \nabla \cdot (k\nabla T) + S_h \tag{3.9}$$

S_h is the source term which includes radiation, volumetric heat sources, and etc. E is the mass averaged energy calculated as the following:

$$E = \frac{\sum_{i=1}^{N} \alpha_i \rho_i E_i}{\sum_{i=1}^{N} \alpha_i \rho_i} \tag{3.10}$$

Where E_i is the phase energy calculated by the specific heat and shared temperature.

The volume transfer between each phase is solved separately. The continuity equation for the volume fraction is used to track volume change:

$$\frac{1}{\rho_i}\left[\frac{\partial}{\partial t}(\alpha_i \rho_i) + \nabla \cdot (\alpha_i \rho_i \vec{v}_i) = S_{\alpha_i} + \sum_{j=1, i \neq j}^{N}\left(\dot{m}_{ji}''' - \dot{m}_{ij}'''\right)\right] \tag{3.11}$$

Where S_{α_i} is the source term of volume, $\dot{m}_{ji}'''$ is the mass transfer rate from phase j to phase i, and $\dot{m}_{ij}'''$ is the mass transfer rate from phase i to phase j. The number of continuity equations to solve will then be $n-1$ (n is the total number of phases) since between each phase there is an interface.

Going back to Table 3.1, to further assist STAR CCM+ to simulate condensation and turbulence, the Evaporation/Condensation and K-Epsilon Turbulence options were chosen. The equations used to calculate such models will be provided in section 3.2 and 3.5.

3.2 Condensation

As mentioned in section 2.4, phase change occurs when latent heat leaves or enters some substance at the specified temperature and pressure. To induce condensation there are two methods in theory: one is to decrease the temperature below the saturated temperature for the given pressure, and two is to increase the pressure for the given temperature. Although it is possible for only one method to be active (usually by controlled experiments), condensation in nature is mostly a combined effort of both methods. The phase change interface can be located at three regions: a wall (when $T_S < T_V$), body of liquid (when T_L average$< T_V$), or vapor cloud. At the phase change interface, there are fluxes of liquid to vapor and vapor to liquid being exchanged constantly as shown in Figure 3.2.
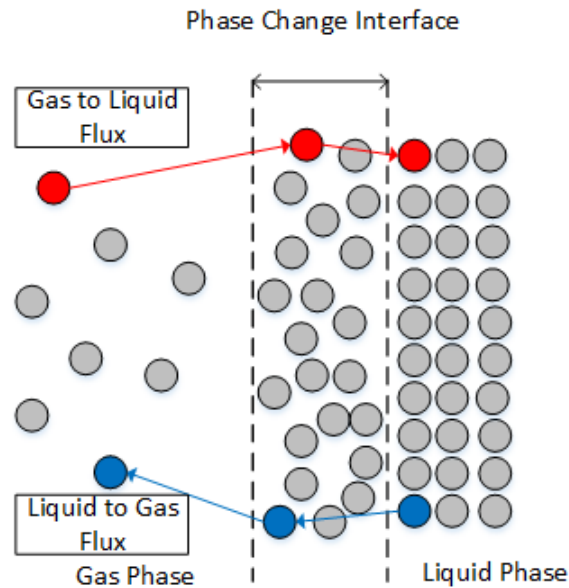
Figure 3.2: The exchange between gas and liquid phase via interface.

When the vapor to fluid flux overcomes the opposed flux, condensation formation becomes observable. However, there is an energy penalty (or may be considered as

energy barrier) that must paid before condensation is formed. The energy penalty is the required energy availability in order for a system to be formed. In thermodynamics, this required energy availability to form a system is than referred to as 'free energy'. Only when the free energy is sufficient enough will condensation form.

For the VOF model in STAR CCM+, enabling the Evaporation/Condensation model will allow the program to recognize the primary and secondary fluid. Three large assumptions are made: the phases are considered to be in equilibrium at the interface, the driving force is the diffusion of species, and the partial vapour pressure of a component in a mixture is equal to the vapour pressure of the pure component at that temperature multiplied by its mole fraction in the mixture [8]. The last assumption is known as Raoult's Law and the equation is the following:

$$P_i = P_i^* f_i \tag{3.12}$$

$$P = \sum_{i=1}^{N} P_i \tag{3.13}$$

Where P_i is the partial vapor pressure, f_i is the mole fraction, and P is the total pressure of the mixture.

The Evaporation/Condensation model starts with defining the evaporation/condensation rate per area for phase i (the secondary phase is phase j):

$$\dot{m}_{ij}'' = -\frac{\rho_i D_i \frac{\partial Y_i}{\partial n}}{1 - \sum_{j=1}^{N_c} Y_j} \tag{3.14}$$

Where D_i is the phase molecular diffusivity, Y_i is the phase mass fraction, N_c is the number of primary phases under phase change, and $\frac{\partial Y_i}{\partial n}$ is the change in phase mass fraction per mole. The mass fraction can be derived by taking the molar

fraction and molar weight into consideration:

$$Y_i = \frac{f_i W_i}{\sum_{j=1}^{N_c} f_j W_j + \sum_{j=1}^{N_s} f_j W_j} \tag{3.15}$$

Where N_s is the number of secondary phases. Although the molar fraction of primary phases under phase change is known, the molar fraction of the non-phase change primary phases are not. To approximate the unknown molar fraction, using the background molar weight (molar weights not at the phase change interface) is another way compensate this value [8]. The background molar weight and molar fraction is defined as the following:

$$W_{bg} = \frac{\sum_{j=1}^{N_s} f_j W_j}{\sum_{j=1}^{N_s} f_j} \tag{3.16}$$

$$f_{bg} = 1 - \sum_{j=1}^{N_c} f_j \tag{3.17}$$

Now replace the unknown terms in Eq. 3.15 with Eq. 3.16 and Eq. 3.17:

$$Y_i = \frac{f_i W_i}{\sum_{j=1}^{N_c} f_j W_j + f_{bg} W_{bg}} \tag{3.18}$$

Phase change mass transfer rate Eq. 3.14 can then be applied to volume transfer equation Eq. 3.11.

3.3 Film/Droplet Flow and Heat Transfer Properties

For vertical dropwise condensation, the droplet will grow and coalesce with other forming neighboring droplets until the mass and size is large enough that the friction of the solid surface, nucleation sites, and droplet surface tension can no longer overcome gravitational forces (drag from prevailing vapor may also cause droplet

release) and permits the enlarged droplet to move in the direction of the over-whelming forces [9]. For highly wetting surfaces, filmwise condensation dominates and covers the wall with a liquid film of some thickness prohibiting direct contact between the wall and vapor. Another form to express condensation on a wall is to consider the balance between the cohesive forces within the condensed liquid and the adhesive forces between the condensed liquid and the wall. If the cohesive force is weak and adhesive force is strong, it is most likely to form a film being highly wetting. On the other hand, if the cohesive force is strong and the adhesive force was weak, a droplet will form as a result.

In STAR CCM+, specific models do exist for the purpose to accurately simulate droplet (Lagrangian Multiphase Models) and film (Fluid Film Model) flow/heat transfer with options of phase change. The issue at hand is that the specific models provided do not collaborate with Eulerian multiphase models. As mentioned in section 3.1.2, Eulerian multiphase was chosen over Lagrangian multiphase to avoid the assessment of tracking particles. In the case for fluid film model, it predicts wall film dynamics for a preexisting film approximated by initial film thickness, assumed velocity, and temperature profile. Unfortunately according to section 5, there is no initial fluid film neither is there any certainty either droplet or fluid film has developed. The only fact is that steam is being condensed on the walls and is accumulated on the bottom of the CNV. Although program wise it may not be possible to specifically model droplet and film flow/heat transfer, the basic theory of how both modes should be explored to assess the possible distortions in the simulation.

3.3.1   Droplet Condensation

The fundamental condition for a non-wetting surface is when the contact angle is $90° < \theta < 180°$. Of course in reality, the wall surface on the microscopic level is never perfectly smooth and the roughness will alter the contact angle. Mate-

rials such as copper, brass, steel, and aluminum have been cured, reheated, and quenched in such a manner that maintaining a smooth surface becomes complicated [9]. Even if it was manufactured to be infinitely smooth, the exposure to surrounding elements quickly degrade fine surfaces. Other sources of contact angle alteration can root from surface inhomogeneity and surface imperfections. Figure 3.3 shows the difference between perfect and imperfect surface contact angles.

SMOOTH SURFACE   ROUGH SURFACE

DROPLET

θ

ϕ

WALL
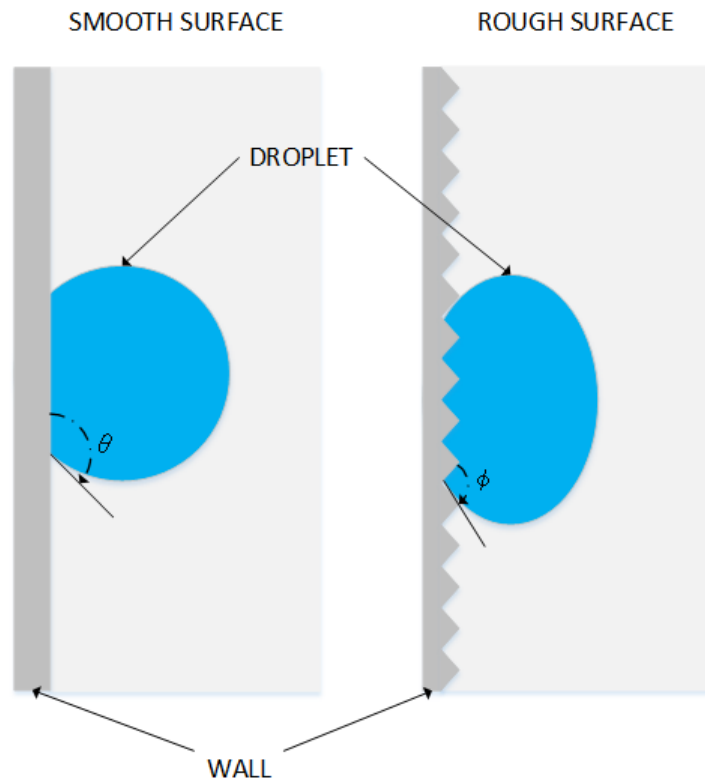
Figure 3.3: Contact angle variation due to surface imperfections.

From Figure 3.3, angles θ and ϕ are clearly not equivalent. In this case the application of the non-wetting condition $90° < \theta < 180°$ becomes insufficient. The rough surface in Figure 3.3 is deformed and the local surface tension of the droplet is further tested to the extreme. Thus wettability must be defined with more delicate

terms. One way is to account for two main parameters: the spreading coefficient (Sp_{ls}) and work of adhesion (w_{sl}) [9]. Sp_{ls} characterizes how a droplet spreads onto a solid surface and w_{sl} is the required work for a droplet to leave the solid surface. With both known, the wettability of some liquid on some solid can be determined. The following equations describe both parameters:

Spreading Coefficient:

$$Sp_{ls} = \sigma_{sv} - \sigma_{lv} - \sigma_{sl} \tag{3.19}$$

Work of Adhesion:

$$w_{sl} = \sigma_{lg} + \sigma_{sg} - \sigma_{sl} \tag{3.20}$$

Where each term is summarized in Table 3.4.

Term	Definition
σ_{sv}	Interfacial tension between the solid and vapor phase
σ_{lv}	Interfacial tension between the liquid and vapor phase
σ_{sl}	Interfacial tension between the solid and liquid phase
σ_{lg}	Interfacial tension between the liquid and low-density gas phase
σ_{sg}	Interfacial tension between the solid and low-density gas phase

Table 3.4: Terms defining wettability

By concentrating on the sign of Sp_{ls}, the property of a droplet can be assessed. When Sp_{ls} is positive, the solid and vapor interfacial tension has overcome other interfacial tension, therefore stretching the liquid droplet to wet the solid surface. If negative, either interface tension σ_{lv} and σ_{sl} or combined was large enough for contact equilibrium to take place.

Assuming a non-wetting solid-liquid interaction, dropwise condensation will start forming as a small embryo as noted in section 2.5. The small embryos will eventually have contact with other embryos coalescing into larger volumes. For a vertical

surface like in section 5, the formed droplet will continue to grow in a relative stationary position until the volume has grown to a point where the gravitational force generated by the increased mass surpasses w_{sl} and vertical motion towards the downward vector is initiated. As the droplet travels, other droplets in its path are removed from their original position or have coalesced with the traveling droplet. Post-traveled paths are momentarily left unoccupied by small embryos allowing new liquid embryos to be formed. Paying attention back to Table 3.3, the convective heat transfer coefficient for condensing water vapor is one hundred times larger during free convection and ten times larger during forced convection compared to liquid water convection. With such large differences, if the objective was to remove heat as efficiently as possible, then it would be favorable to continuously have condensation.

In terms of equations based on dropwise condensation, there are various theories attempting to approximate bubble size, temperature gradients throughout the bubble, and heat transfer coefficients. One theory is to consider that there is numerous sites on some surface and condensation can only be formed from these sites. The non-wetted space on the surface cannot form condensation until droplets coalesce and cover more surface area. Another theory is to consider that condensation is first formed as a micro film across the surface with thickness in microns. When the thin film is broken, droplets will form. Both introduced concepts were conceived around the 1930's and to go into detail would be outside the scope of this research. More information can be found in the references section ([25] and [26]).

3.3.2   Film Condensation

When the contact angle is $0° < \theta < 90°$, the liquid formulation on the solid surface is determined to be wetted. If it fully wets the surface, it eventually will develop into a film. Since the surface is constantly covered, the thin fluid film prevents

direct contact between the vapor phase and solid surface making a temperature differential such that the fluid film temperature (T_L) is hotter than the solid surface (T_S) but colder than the vapor (T_V). Assuming a vertical wall, fluid film will start from the point of onset and as the film is flowing down the wall the thickness gradually increases (illustration given in Figure 3.4).
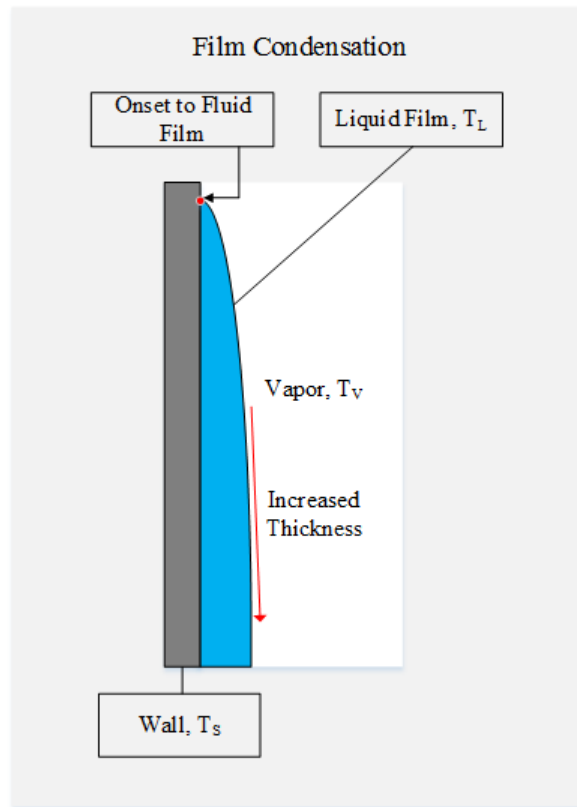
Figure 3.4: Film condensation diagram.

The flow downward is continuous being supplied with new condensate from the point of onset and phase change from the fluid/vapor contact. When visualizing condensation flowing downward, for a moment of time, the point of onset does un-wet but will immediately re-wet with new condensation. In this manner, the point of onset is repeatedly being supplied with new condensate.

The heat from the vapor can only be transported to the cold solid surface via phase change by direct contact between solid surface and vapor (however available surface area is limited) and phase change on film surface or convection between fluid and vapor added with convection and conduction between the wall and film. Considering Eq. 3.1 and Eq. 3.3, the larger the temperature difference, the more heat that can be transferred and therefore the load of phase change per time is increased. With T_L being higher than T_S, the temperature difference between T_L and T_V is smaller than the difference between T_S and T_V providing degraded levels of phase change compared to the maximum potential.

Unlike droplet condensation, film condensation can be characterized analytically without idealizing the shape of the condensate (droplet theories highly depend on spherical droplet assumptions). The two common analytical analyses which presumes laminar film flow would be integral and boundary-layer methods. Integral methods uses the force balance between gravity and viscosity to express the velocity profile for a certain height. Given the main mode of heat transfer is conduction, combining the heat transfer across the film and integrating the velocity throughout the whole film thickness will yield the height dependent film thickness which can be utilized to find the average Nusselt number. The boundary-layer method uses the COm, COM, and COE with assumed boundary conditions to build similarity variables formulating the local Nusselt number. Table 3.5 shows the base assumptions for both methods.

Integral	Boundary Layer
Laminar Flow	Same
Constant Properties	Same
Subcooling of liquid is negligible	Same
Inertia effects are negligible	N/A
Vapor is stationary	N/A
No shear between liquid and vapor interface	Same
Heat transfer in film is limited to conduction	N/A
N/A	No slip condition
Constant wall temperature	Same

Table 3.5: Assumptions for film condensation integral and boundary-layer analyses [9].

For STAR CCM+ similar to the VOF model, fluid film model uses the same mass, momentum, energy conservation but specific only to the liquid phase. The film source and sink term serves to add or subtract film volume at the specified location and boundary condition.

3.4   Condensation with Non-Condensable Gas

One of the prominent complications in inducing condensation is the presence of non-condensible gas. Let's say there is a container filled with a non-condensible gas. The container has room temperature isothermal walls and an inlet valve that injects water vapor at some velocity but no outlet anywhere to release fluids. As pointed out in section 3.3, phase change from vapor to liquid requires an increase in pressure and/or a decrease in temperature. Assuming the pressure build up in the container is small enough to be negligible and the mixing between the non-condensible gas and vapor are immiscible with very slow heat transfer, the main mechanism to cool the vapor and liberate heat is direct contact with the isothermal

wall. While the vapor is being injected, the vapor spreads throughout the internal volume of the container in some turbulent fashion. The sudden issue in hand is that a portion of the preexisting non-condensable gas remains roaming around the isothermal wall preventing the vapor from having direct contact. If the initial preexisting gas was condensible, the condensation of the gas would form on the wall and accumulate on the bottom without existing as a gaseous film. With the non-condensible gaseous film, water vapor cannot condense on the wall and severely limits the efficiency of phase change. Another possible obstruction of vapor heat transfer is covering the water vapor condensation by the non-condensable gas which prevents again contact with lower temperature entities. Figure 3.5 illustrates both circumstances.
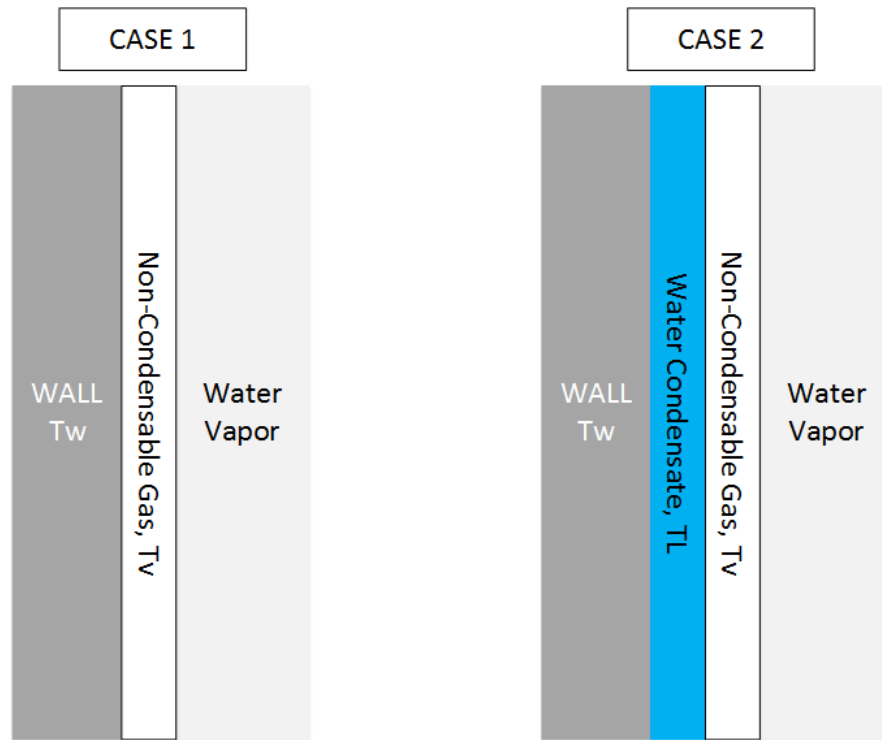
Figure 3.5: The development of non-condensable films with immiscible fluids.

The inserted fluid and preexisting gas does not necessarily be immiscible for non-condensing gas to cause issues. Let's say the injected water vapor and preexisting gas were well mixed beyond recognition before making direct contact with the surrounding wall. When the fine mixed gas makes contact with the wall, the water vapor portion of the gas mixture starts condensing on the wall and gas separation is initiated. Since the preexisting gas is non-condensable, the gas separation then forms a two-layer fluid structure (water condensation over the wall with non-condensable gas blanket surrounding it) over the wall identical to the immiscible version preventing heat transfer.
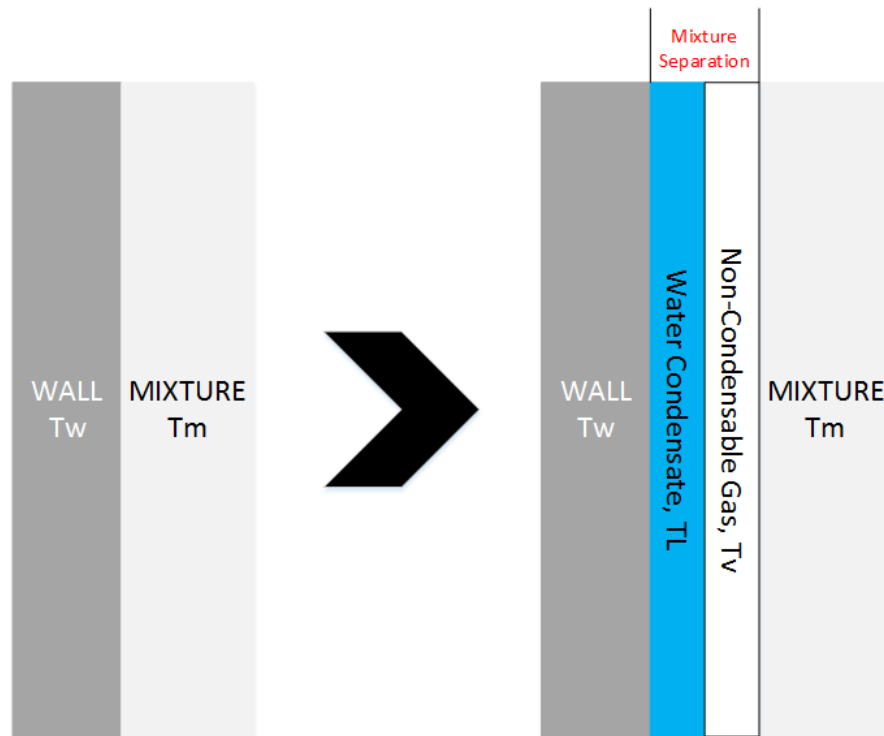
Figure 3.6: The development of non-condensable films with miscible fluids.

Now turning back to STAR CCM+, for reasons that will discussed in section 6 the effect of non-condensable gas was large and becomes one of the obstacles in simulating condensation in large volumes.

3.5 Turbulence

Turbulence is the transport of momentum with complex motion which appears to be chaotic and random. Although it would be preferable to begin solving for turbulence from the well known Navier Stokes (NS) equation, the movement of the flow element and the proportional relationship between the stress and velocity gradients can no longer be sustained. Terms such as the velocity must be redefined to account for the rapid differential change in space and time. The most common method to characterize turbulence and enable NS is to consider the unperturbed flow to be smooth with predictable streamlines and averaged properties. The random movements added to the unperturbed flow are then identified as fluctuations that can be superimposed. The measure of turbulent flow influence to the unperturbed flow can be quantified via the fluctuated terms. The instantaneous value of some flow quantity is given in equation form in Eq. 3.21 and is illustrated in Figure 3.7.

$$a = \bar{a} + a^{'} \tag{3.21}$$

Where $\bar{a}$ is the time averaged and $a^{'}$ is the fluctuation of flow quantity a. The time averaged values are defined in Eq. 3.22.

$$\bar{a} = \frac{1}{\tau} \int_{t_0}^{t_0 + \tau} a \, dt \tag{3.22}$$

Where t_0 is the initial time and τ is the time elapsed.
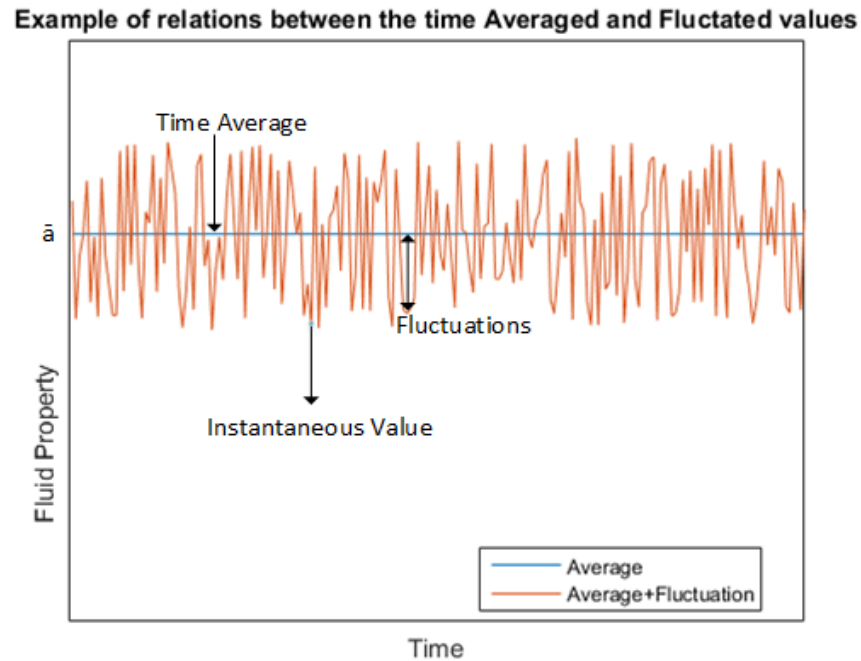
Figure 3.7: The relation between time averaged and fluctuation values.

The two points to make note of are that the mean value $\bar{a}$ time integral has to be sufficiently long to be independent of time and the time average of fluctuation term $a^{'}$ must be zero. This interpretation allows the following mathematical rules to be valid:

- The average of the sum of instantaneous quantities is equal to the sum of the averages of the individual instantaneous quantities.

- The average of the product of instantaneous quantities is equal to the product of the individual instantaneous quantities.

- The sum and product of the averages of the individual fluctuation terms is zero.

- The average of the sum and product of fluctuation terms may or may not be zero.

The uncertainty of whether the average of the sum and product of fluctuation terms are zero roots from how each turbulent term can differ throughout the time interval. If the fluctuations were truly random, then in any given time the probability for fluctuations to be equivalent for two variables (however same units) would be small. For the sum and product to be zero would suggest that the flow is other than turbulent. For example, the two-dimensional Cartesian coordinate advective term in NS can cast light on the fluctuation terms. The following is the tensor notation of the advective terms in NS:

$$Adevective = \frac{\partial}{\partial x_i}\left(u_j u_i\right) \tag{3.23}$$

Velocity terms at an instantaneous time in Eq. 3.23 will be replaced with the time average and fluctuation terms as shown in Eq. 3.21:

$$= \frac{\partial}{\partial x_i}\left[\left(\overline{u_j} + u_j^{'}\right)\left(\overline{u_i} + u_i^{'}\right)\right]$$
$$= \frac{\partial}{\partial x_i}\left[\overline{u_j}\,\overline{u_i} + \overline{u_j}u_i^{'} + u_j^{'}\overline{u_i} + u_j^{'}u_i^{'}\right]$$

Averaging this will yield the following:

$$\frac{1}{\tau}\int_{t_0}^{t_0+\tau}\frac{\partial}{\partial x_i}\left(u_j u_i\right)dt = \frac{\partial}{\partial x_i}\left[\overline{u_j}\,\overline{u_i} + \overline{\overline{u_j}u_i^{'}} + \overline{u_j^{'}\overline{u_i}} + \overline{u_j^{'}u_i^{'}}\right]$$

Going back to the mathematical rules developed, some terms can be replaced and canceled:

$$= \frac{\partial}{\partial x_i} \left[\overline{u_j u_i} + \overline{u_j} \overline{u_i'} + \overline{u_j'} \overline{u_i} + \overline{u_j' u_i'} \right]$$
$$= \frac{\partial}{\partial x_i} \left[\overline{u_j u_i} + 0 + 0 + \overline{u_j' u_i'} \right]$$
$$= \frac{\partial}{\partial x_i} \left[\overline{u_j u_i} + \overline{u_j' u_i'} \right]$$

Notice that if $\overline{u_j' u_i'}$ was zero, then the advective term will remain in its averaged form of $\frac{\partial}{\partial x_i}(u_j u_i)$ with no turbulent terms. By applying the same analysis to the full NS equations, the turbulent version of NS can be obtained:

$$\rho \left[\frac{\partial \overline{u_j}}{\partial t} + \frac{\partial}{\partial x_i} \left(\overline{u_j u_i} + \overline{u_j' u_i'} \right) \right] = -\frac{\partial \overline{P}}{\partial x_j} + \mu \nabla^2 \overline{u_j}$$

$$\frac{\partial \overline{u_j}}{\partial t} + \overline{u_i} \frac{\partial \overline{u_j}}{\partial x_i} = -\frac{1}{\rho} \frac{\partial \overline{P}}{\partial x_j} + \frac{\partial}{\partial x_j} \left(\frac{\mu}{\rho} \frac{\partial \overline{u_i}}{\partial x_j} \right) + \frac{\partial}{\partial x_j} \left(-\overline{u_j' u_i'} \right) \qquad (3.24)$$

The collaboration between NS and turbulent theory is called the Reynolds equation (in STAR CCM+ it is known as the Reynolds-Stress Navier-Stokes and shown in Table 3.1) and the newly implemented average fluctuation term on the left hand side of Eq. 3.24 is then recognized as the Reynolds stresses which represents the transport of momentum due to turbulence.

The theory of using averaged and fluctuated components are not limited to turbulence. The theory itself is to describe flow statistically with pseudo randomness (there are a couple of parameters that can be controlled). Solving flow in such a manner will accompany uncontrollable statistical error that would not have existed if solved analytically or numerically. Still even with the generalized theory and the enormous effort that must be made to solve it, turbulence can be much more complicated in levels that surpass the capacity of the introduced theory. The complexity of the Reynolds equation stems from the increased number of intro-

duced unknowns. When $j = 1, 2, 3$ (in tensor terms, numbers 1, 2, and 3 represent the three dimension system), Eq. 3.24 can be set into three equations for each given dimension. The unknown components is then the averaged velocity in three directions, the mean pressure, and the six combinations for the average fluctuation terms. At this point including the three turbulent NS equations and conservation of mass, there are four equations to solve for ten unknowns. This is the dilemma for turbulent equations as numerous closure relations must be implemented. To reduce the number of unknown variables, the fluctuation terms are replaced with other unknown variables using the Boussinesq relationship. The turbulence model (closure relation model) chosen from STAR CCM+ was the k-epsilon model. To be specific, the Realizable k-epsilon model and for reasons that will be provided in section 6, no other models were chosen. The k and epsilon (ϵ) represent the turbulence kinetic energy and turbulence dissipation rate and are scalar values. By making the Boussinesq relationship added turbulent NS equations about a scalar, NS equations for both k and ϵ can be obtained. The determination of the newly created constants within both NS equations is the point where various models and assumptions exist to solve the turbulent problem. Once k and ϵ are determined, the fluctuations can calculated.

Chapter 4: Test Facility Description

Before going into details on what kind of procedures were used on NIST-1's facility experiment (the data to be used to validate the heat loss simulation is produced through this particular experiment which will be further discussed in section 5), a comprehensive description of NIST-1's history and components is essential. Due to a Nondisclosure Agreement (NDA), only portions of the relevant components will be revealed.

4.1   NIST-1 Facility

NIST-1 is the successor of the MASLWR test facility. MASLWR was built in 2003 as a scaled-down version of NuScale's natural circulation driven SMR without using nuclear fuel. The original design was conceived jointly by Idaho National Engineering and Environmental Laboratory, OSU, and NEXANT-Bechtel between the year of 2000 and 2004 (shown in Figure 4.1) [6].
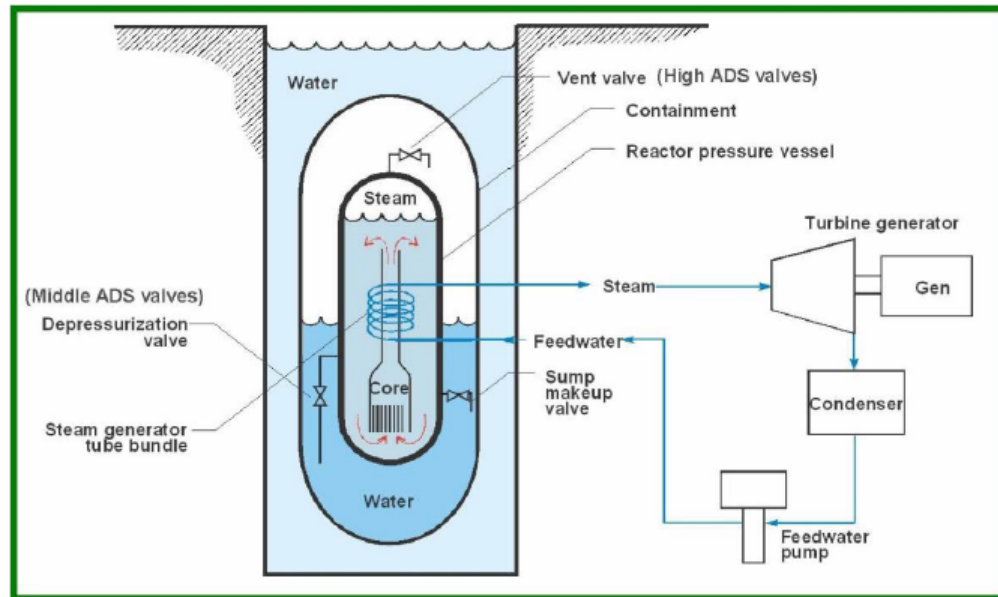
Figure 4.1: MASLWR Conceptual Design Layout [6]

It was installed in OSU as a proof-of-concept system for natural circulation driven reactors. The added heat from fission in the actual nuclear reactor is accurately simulated in MASLWR by using multiple electrical heat rods making the test facility a non-nuclear structure. Although data for normal operations of the SMR can be extrapolated from fellow PWR facilities as well as be obtained from the MASLWR facility, the effectiveness of natural circulation cooling during accident scenarios is mostly uncharted territory. To supply data for accident scenarios, data generated from MASLWR aids the verification and validation process of the thermal hydraulic codes for the NuScale SMR that will later be used to simulate and analyze for situations requiring further exploration.

To better reflect NuScale Power's SMR design, MASLWR was officially shutdown in 2014 and reopened as NIST-1 in 2015 with extensive modifications. NIST-1 can be subdivided into the following six main components:

- Primary Circuit: The primary acts as the main heat source. Elements such as the 400 kW core, the hot leg riser pipe, pressurizer, shell side of helical coil SG, and cold leg downcomer annulus.

- Secondary Circuit: The secondary acts as the main water source. Elements such as the feedwater storage tank, main feed pump, tube side of helical coil SG, main steam line, and outlet.

- Automatic Depressurizing System: Consists of break lines that are used for accident testing of reactor vent lines ADS lines and sump return lines.

- Containment Vessel: Used to contain steam. Rated to 810 psig to contain steam released through reactor blowdowns.

- Cooling Pool Vessel: An open tank of water that stretches the full height of the CNV, and acts as its heat sink.

- Heat Transfer Plate: A heat transfer medium made out of stainless steel plate between the CNV and CPV.

4.2   Reactor Pressure Vessel (Primary Loop)

The RPV is a constructed stainless vessel and has a maximum operating pressure of 1650 psig at $630°F$ [7]. The internals of the NIST-1's RPV is identical to the NPM's RPV as described in section 1.1. Upper and lower plenums, the position of the PZR, and baffle plates function to imitate the NPM at scaled values. As the position of the core in NPM is shown in Figure 1.2, NIST-1 has installed electrical heaters at the similar position. The PRZ has its own set of electrical heaters to regulate the static pressure in the RPV.

4.3 Secondary Loop

The secondary loop purpose is to supply water from the water reservoir to the heat exchanger via main feed pump, vaporize secondary loop water, and transport the superheated steam to the CNV. As mentioned in section 1.1, the helical coiled heat exchanger acts as a primary external coolant and is the main contraption to produce superheated steam in relatively small allotted space. For accurate data generation, NIST-1 uses helical coils as heat exchangers. The benefits coiled geometry is the substantial increase in total surface area. With increased heat transfer area, the heat exchanger efficiency can be enhanced regardless of the limited heat exchanger space. The rate of superheated steam production can be carefully controlled by adjusting the secondary loop pressure and feed flow rate.

4.4 Containment Vessel

The CNV is a stainless steel container meant to store steam produced by the secondary side. The CNV in NIST-1 represents the vacuum cavity that in-houses the RPV in the NPM. The high maximum pressure allows for superheated steam to be condensed at higher temperatures. Multiple steam injection and recirculation valves are located around the CNV.

4.5 Heat Transfer Plate

The HTP is a stainless steal plate physically in between the CNV and CPV. In the NPM, the CNV is submerged in the cooling pool transferring heat to the ultimate heat sink. To characterize the heat transfer between the CNV and cooling pool, the HTP size in NIST-1 has been scaled accordingly.

4.6   Cooling Pool Vessel

The CPV acts as the ultimate heat sink cooling pool in NPM. The CPV is a large cylindrical tank of water open to the ambient atmosphere. To add structural integrity, the tank walls are thicker on the lower portion than the upper portion while maintaining the same inner wall diameter throughout the whole height.

4.7   NIST-1 Insulation

The insulation is 3 inches thick made out of fiberglass called Eslin with material properties in Figure 4.2.

Insulation Thermal Properties		
Trade Name:	E-Glass Fiber	
Manufacturer:	Eslin	
Type:	Fiberglass	
Dry Density:	12.5 lbm/ft³ (200.2 kg/m³)	
Thermal Conductivity:	Temperature (°F,°C)	$k \left(\frac{BTU*in.}{h*ft^2*°F}, \frac{W}{m^2*°C} \right)$
	100/38	0.220/0.032
	200/93	0.292/0.042
	300/149	0.330/0.048
	400/204	0.380/0.055
	500/260	0.420/0.060
	600/316	0.480/0.069
	700/371	0.520/0.075

Figure 4.2: Properties of Eslin E-Glass Fiber Insulation [7]

4.8 Affiliation with NuScale

Although NIST-1's sole purpose is to run and generate data for NuScale Power's hydraulic codes, NIST-1 remains independent from NuScale Power. As discussed in section 1.1, NuScale Power has to provide proof of concept to surpass every regulation set by the NRC. NIST-1 must exist as an independent entity free of bias regardless if the generated data contradicts NuScale Power's models. The relationship between NIST-1 and NuScale Power is restricted to financial support, providing test details, and the authority to run tests. NuScale Power has the right to refuse data if the data was deemed to be faulty and requires to be rerun. NIST-1 ensures its credibility by receiving routine audits from third party organizations and from the NRC itself.

Chapter 5: Experimental Test Setup of HP-16b

Due to the confidentiality of facility dimensions, scaling parameters, and test data all numerical information will be described as symbols. As NIST-1 performs multiple test for NuScale Power, the High Pressure (HP) series tests long term cooling and accidents concerning flow loss and line breaks at high pressures. HP-16b represents testing of the CNV heat loss at various internal fluid temperatures [10]. Corresponding to the variant internal fluid temperatures, the specified CNV peak pressure changes according to experienced temperature levels. For HP-16b, the most critical parameters were determined to be CNV wall and fluid temperatures, CNV and secondary side pressures, CNV water level, flow into the CNV, and ambient temperature conditions before each data collection. To solely concentrate on the heat loss of the CNV, the HTP wall surface was covered with silicon layers to prevent heat from leaving the CNV via HTP. The initial conditions are on the primary and secondary are in Table 5.1.

Parameter	Value
Core Total Power	A kW
RPV Pressure	Steady B psig
Feedwater Flowrate	C lbm/min
Steam Pressure	Steady D psig
Secondary Steam	Steady with saturated or superheated steam

Table 5.1: Suggested RPV and secondary side conditions [10]

The CNV will be preheated and the initial internal pressure will be a vacuum relative to ambient pressure. After the initial conditions on the primary and secondary are met, superheated steam is injected from the spray line located on top of the

CNV. To reach the specified CNV pressure, superheated steam is carefully continuously injected. While the HTP on the CPV side has been insulated to isolate heat loss in the insulation, the CNV left with the injected superheated steam will condense and lower the internal pressure. Once the data collection is done, the CNV is drained and the relative pressure is back to initiate the next superheated steam into the CNV. The steam injection is repeated seven times with different CNV peak pressures set. Table 5.2 shows the different CNV peak pressures.

Data Point	CNV Peak Pressure (psig)	CNV Preheated Wall Temperatures (°F)
1	P1	T1
2	P2	T2
3	P3	T3
4	P4	T4
5	P5	T5
6	P6	T6
7	P7	T7

Table 5.2: HP-16b Data Point Conditions (where P1<P2<P3<P4, P1=P7, P2=P6, and P3=P6) [11]

The following is the simplified procedure conducted in the actual test:

1. Start up the data acquisition system.

2. Start pulling vacuum from CNV and turn on wall heaters to meet pre-heat CNV temperatures.

3. Turn on electrical heat rods and start producing superheated steam.

4. Meet primary and secondary initial conditions.

5. Inject Superheated Steam and build pressure.

6. Stop injection and allow for natural CNV cooldown and depressurization for X (actual number will not be revealed) hours.

7. Release pressure and drain the CNV.

8. Once pressure has decreased and CNV wall preheated temperature is completed, inject superheated steam to build pressure to the next data point.

HP-16b was successfully completed October 25, 2016 and the intent of the test was approved by NuScale Power.

Chapter 6: Simulation

This chapter is dedicated to describing the simulation setup, environment, and associated theory. As mentioned throughout the thesis, one section in this thesis is reserved for explaining the details on the complications of modeling the full simulation with fluid regions.

6.1 Physics Exclusion Process

6.1.1 Superheated Steam Injection System and Turbulence

The superheated steam injection system is located at multiple locations on the CNV. The spray line used in HP-16b is located on top with a pipe insertion length of a few inches long into the CNV with holes drilled onto the side (the tip is covered). The concept is not to have the superheated steam just fill the void but spread on the CNV inner wall to efficiently induce condensation and cool the system. Having the exact dimensions being an obvious prerequisite, other points to guarantee is whether the injected superheated steam in spreading as intended. Since it is the vapor phase being injected, it is most certainly turbulent flow. As mentioned in section 3.5, multiple turbulent models exist for any CFD program. The major issue is not only determining which turbulent model best fits the experiment but also determining which tuning parameters to use and what values will provide a converging stable solution. With trial and error, the transient effects will have to be tested to find the best fitting model. The initial limiting factor is the size of the mesh for the given volume. To reflect the vorticity and turns in the flow it is required to have smaller meshes. If the volume is large

compared to the required mesh size to accurately model turbulence, the transient solution is slow. It is one thing to make the mesh excessively small at boundaries but it is another to have mass fluid regions to be small as well. Without access to a cluster or supercomputer, the process of verifying turbulence models becomes too time consuming with no guarantees.

6.1.2   CNV Wall Condensation

During and after superheated steam injection, the relatively subcooled CNV wall removes latent heat from the steam inducing phase change. The unfortunate decision that has to be made is whether dropwise or film wise condensation is taking place. The CNV is made out of a type of stainless steal and can be regarded to be either depending on the chemical composition and surface geometry. Since there are no visual ports installed on the CNV, there are really no direct method to verify. One indirect method could be to track the transient water level in the CNV at each time to check if the correct combination of condensate production and condensation transport is in progress. However even with water level justification, condensation type cannot be determined. As discussed in sections 3.3 and 3.3.1, depending on which type of condensation can variate the type of physical model that can be used. Using CNV wall and HTP known temperatures as the final validating step, trial and error becomes the major player in determining which type of condensation to expect and which models are valid. Another complicated issue is the mesh size. With mesh sizes relatively much larger than the condensation film thickness or droplet diameter, the simulation has the potential to exaggerate condensation amount or not have condensation at all due to cell averaging properties. Figure 6.1 shows the influence of smaller mesh sizes.
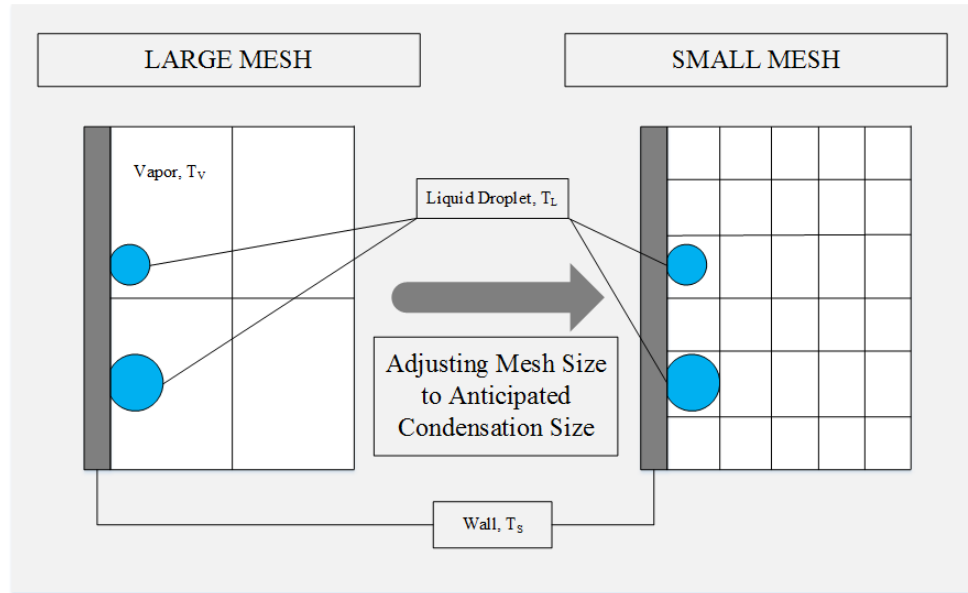
Figure 6.1: The difference between well- and ill-sized mesh.

Similar to section 6.1.1, the required mesh size is in the scale of millimeters for a huge volume with wide surfaces areas. For a transient solution with time steps of 0.05 seconds (still large considering the Courant number) for a minimized version of the CNV as a test run, it took more than ten minutes for a single time step to converge to a moderate criteria. When taking both condensation type determination and mesh size requirements into account, condensation simulation alone is a respectable topic for research.

6.1.3 Pressure Buildup

The pressure buildup can be attributed to the superheated steam injection during the experiment. As there are no heat sources other than the steam in the CNV, the pressure after injection procedures is unable to be higher. Although pressure is one of the known parameters and data is available, the accurate simulation of

pressure buildup can be complex due to the close links with sections 6.1.1 and 6.1.2. Actions for pressurization would be steam injection and depressurization would be condensation. If the pressurization (spray line and turbulent modeling) and depressurization (condensation) are the correct balance, the pressure throughout the simulation should accurately mimic the facility instrument data. Nonetheless, pressure buildup validation is an essential part of determining the heat loss in the CNV.

6.1.4 Collective Complexity

Sections 6.1.1, 6.1.2, and 6.1.3 are major obstacles that cloud the true objective of this thesis. All previous efforts are to accomplish one thing, to correctly justify the right amount of heat transfer entering the CNV wall. The heat leaving the wall can be simulated by placing insulation around the CNV as in NIST-1 with the correct thickness. As a disclaimer, there are other structures that are attached to the CNV acting as supports to keep NIST-1 intact in cases where structural stresses are enough to deform entities and also to prevent heat transfer between the CNV and CPV via the CNV wall. but are not added to the CFD geometry due to lack of information. On the outside of the insulation is ambient air which slightly changes as the RPV's heater rods are powered up. Thus it is relatively simple to model the heat leaving the CNV (CFD is still required since it is three dimensional convection and conduction).

All in all to assess the right amount of heat transfer leaving the CNV system, every phenomenon governing the heat transfer into the CNV becomes imperative. The conclusions of sections 6.1.1, 6.1.2, and 6.1.3 point to eventual trail and error methods using CNV and HTP known temporal temperatures as the measure of how well the simulation reflected the experiment. Considering the CNV to be several meters high with a wide radius, the time required to solve the whole solid and fluid region with mesh sizes adjusted for turbulence and condensation model-

ing with moderate time steps to ensure stable converging simulations (the STAR CCM+ license and computational power given to students is limited. There is a high performance computing cluster for the College of Engineering where computational time and power is evenly distributed among various engineering departments with high computational demands that will solve CFD exponentially better) would take more than months if not years.

6.1.5   Final Decision

With the facts and the given time for masters thesis, the grand decision was made jointly by the author and academic advisor to simplify the simulation by solely using the solid region. One side of the CNV will be the thermal boundary condition and HTP wall temperatures will be reserved for comparison (there are no TC in the insulation and insulation temperatures cannot be used as a point of reference).

6.2   Geometry Modeling

The steps to starting CFD simulations are comprised of geometry modeling, meshing, physical phenomena modeling, and data comparison. An ideal CFD program would be capable to do the first three steps to the highest quality. For STAR CCM+, geometry modeling and meshing is not of the best quality nor as user friendly as compared to other specialized programs. For this purpose, the geometric modeling of the CNV, HTP, and insulation were done in SOLIDWORKS. The position and dimensions were based on the the most current Facility Description Report at the time. Although SOLIDWORKS has its own unique file format, the geometry file can be exported as a parasolid file which can imported to other programs.

6.3   Mesh

From the exported parasolid file from SOLIDWORKS, it can be imported to STAR CCM+ or any other program with meshing capabilities. To minimize the number of programs used, an attempt was made to mesh the SOLIDWORKS geometry. Despite setting the mesh size to be large enough to compile quickly and small enough so the original geometry was not deformed, it took STAR CCM+ more than an hour to mesh with unacceptable quality. Further fining the mesh only led to compile errors. Given this situation, meshing was immediately transitioned to ANSYS. Without any specification on what kind of mesh to use or size, ANSYS will mesh the imported geometry according to the shape. For example, flat surfaces and cylindrical geometries are given mapped meshing while spherical and conic geometries are given tetrahedral meshes to accommodate the curved surfaces. If there is no restriction to what kind of mesh must be utilized, this automatic is meshing is typically acceptable. By specifying the maximum mesh size, a more fine mesh can be generated as a whole. For locations such as boundary condition locations, the mesh can be refined locally. As explained in section 6.1, the fluid region was excluded and as a result more than 50% of the volume was removed. With no ties to the fluid region, there is no need to make the mesh fine within the volume for turbulence and at the CNV walls for condensation (however boundary condition locations should be relatively finer than the rest of the geometry to ensure quality simulations). To ensure spatial grid convergence, three sizes were tested under three different time steps and details are provided in section 7.2.

6.4 Simulation Setup

6.4.1 Physical Model Setup

Confined to solid regions, the physical models from STAR CCM+ are then as shown in Table 3.2. The selection of constant density implies that material deformation, phase change, or any physical stress that impacted the CNV and HTP structure was ignored. The 'solid' option in STAR CCM+ is for single component materials. From section 4 it can be seen that at least two materials exist; stainless steel and e-glass fiber. To accommodate with multiple material properties, two separate solid regions were specified for each material. The complications for such modeling is the communication between each region. If there was only one region, the system regards any structure to be part of the same drawing and information such as mass, energy, and other continuum quantities is reflected from one cell from one structure to the next cell in another structure without any additional settings. With two solid regions, interfaces between boundaries need to be created manually [8]. Figure 6.2 illustrates how interfaces are recognized.
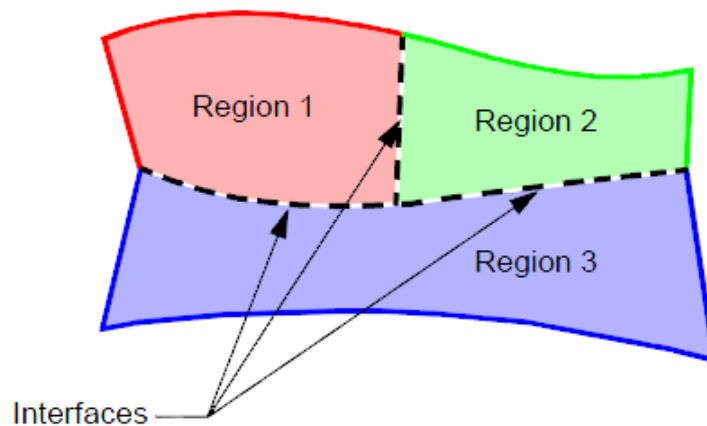
Figure 6.2: Coincident boundaries between each region creating interfaces that are represented as black dotted lines [8].

For heat transfer between solid-solid regions, interface creation is essential. If it is possible, the STAR CCM+ system is better utilized when minimal interfaces are created to minimize communication error between multiple regions. As long as the phase of the material and applied physics remains the same, the number of regions should be restricted.

To restrict the number of regions in the case of this thesis, the 'multi-solid' model option would have been best since multiple materials can be specified for by parts in the geometry without defining new regions. The only reason the multi-solid model was not selected was due to the fact that STAR CCM+ cannot recognize imported geometries from other programs as a structure with individual parts. What STAR CCM+ does see is the imported geometry as one whole object with multiple boundaries that must be defined. As an alternative method to assign different material properties, defining multiple regions was the only method available other than recreating the geometry in STAR CCM+.

6.4.2   NIST-1 HP-16b Data Import

As mentioned in the first sentence in section 5, the experimental data is proprietary. Due to the proprietary nature of NIST-1's experimental data, storage and export of data is strictly controlled. The export of data requires confirmation from various managers in NIST-1 and in NuScale Power. With the NDA, observing and analyzing data from the designated portal is allowed. To import and analyze data on a public or private computer is typically impossible if there is no physical method to transport the data. Since this thesis is of low priority to NIST-1 and NuScale Power, an alternative method was chosen to make CFD simulations possible. First, a finite number of data points that are located at the local maxima and minima were saved at the secure portal in a EXCEL file via MATLAB. By taking a picture of the data points, they can be manually imported into another computer. The imported data points can be used to create new data points in

between by using MATLAB's cubic fit to curve functions. Due to the nature of curve fitting, data points that are not of imported origins do not fit the actual data points exactly but follow the trends at roughly the same time steps. For this reason, the data simulated from this thesis do retain discrepancies compared to the actual data. To make things clear, the comparison will be upon the fitted data.

6.4.3   TC Locations

TC locations are placed on ten distinct heights for the HTP and five for the CNV. Since only five are available for the CNV, only TCs on the same height on the HTP have been collected. The locations are in the following figure:
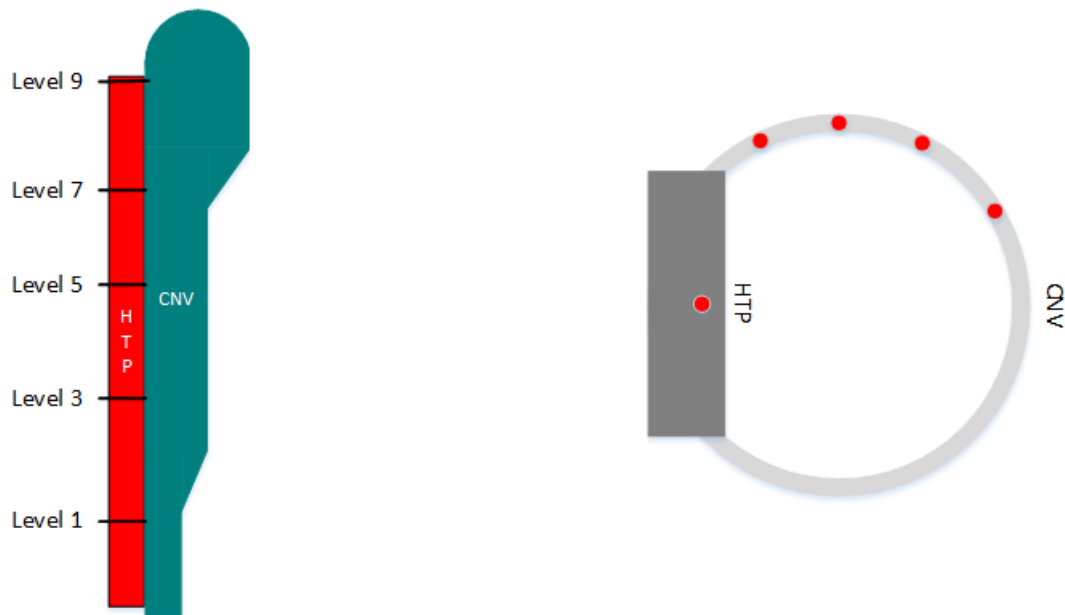
Figure 6.3: TC locations on the CNV and HTP

6.4.4   Boundary Condition Setup

The TCs installed in NIST-1 are in sets categorized by height. The categories are from level 0 (lowest positioned TCs) to level 9 (highest positioned TCs). The CNV has TCs at odd numbered heights and the HTP has TCs at all ten heights. Since the heat transfer from the CNV wall to the insulation is paramount, the thermal boundary conditions that supply experimental data to the CFD simulation is placed at the inner wall surface of the CNV. Although the CNV inner surface was chosen, the wall TCs are not actually at the surface of the wall but inserted into the CNV at some depth. Due to not being able to place boundary conditions at the specific depth, the CNV temperatures were placed at the CNV inner where boundary conditions can be set. The restriction of only five temperature measurements for the whole height of the CNV poses an issue when information between the known data points are required to supply boundary conditions. By importing a matrix of experimental CNV wall temperatures with x, y, and z coordinates with the time stamp included, STAR CCM+ can automatically interpolate/extrapolate from the given data positions and select the data point that is closest to the desired boundary condition to solve the finite imported data issues. Since according to Figure 6.3 only four TCs exist on the west side of the CNV, the decision was made by the author to average all temperatures on the four TCs and use that value azimuthally for the whole CNV inner wall for that height. The primary reason for such actions is that since STAR CCM+ will attempt to place interpolated or extrapolated values on the inner CNV wall based on only four known points on every given height, it could potentially yield non-realistic values. A similar analogy can be made when trying to calculate steam properties. If one attempts to extrapolate specific volume at temperature 400°F with only two known points at 40°F and 80°F, then the calculated value will be extremely different than using points between 405°F and 395°F.

However since the CNV wall is wide with potentially having a non-isothermal

inner wall distribution, the following plots are given to investigate how they differ using actual NIST-1 experimental data from HP-16b:
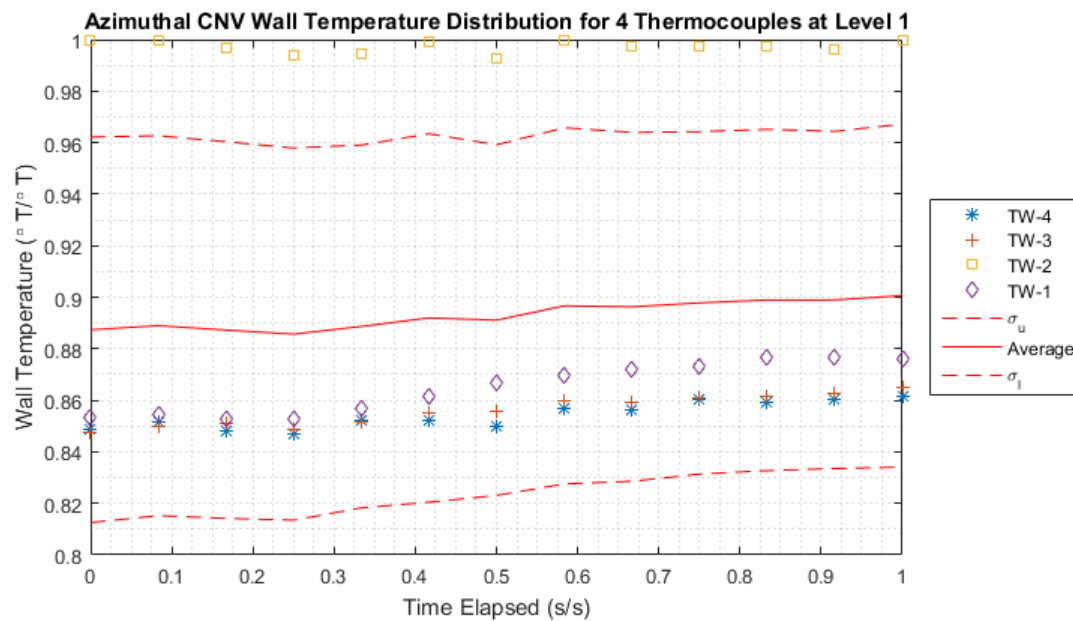
Figure 6.4: Temperature distribution in time for the four CNV TCs with the average and standard deviation values at level 1 (normalized in temperature and time).
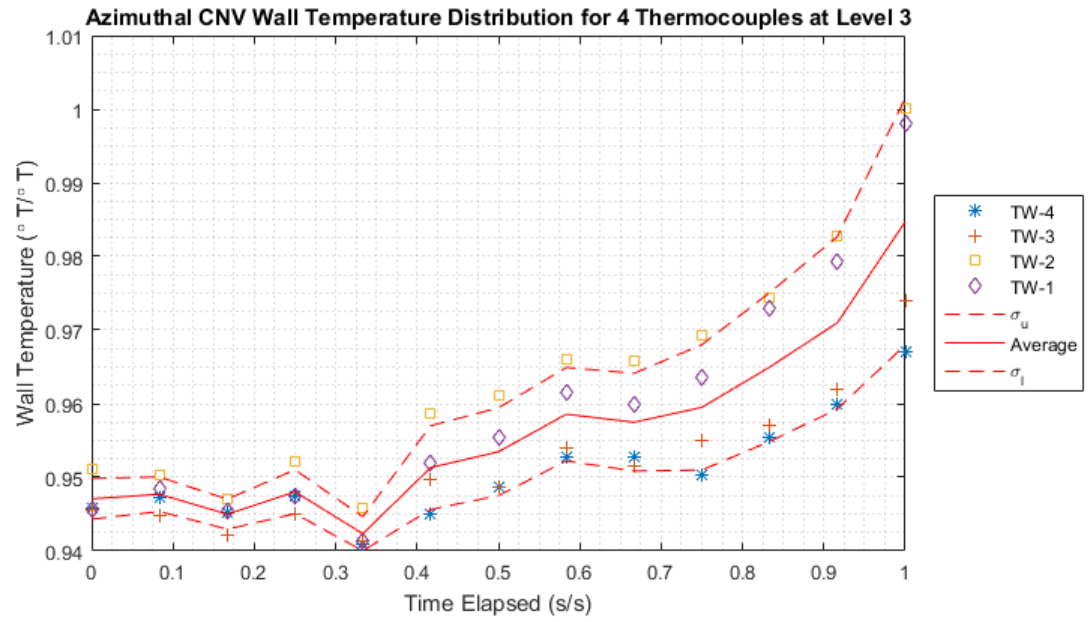
Figure 6.5: Temperature distribution in time for the four CNV TCs with the average and standard deviation values at level 3 (normalized in temperature and time).
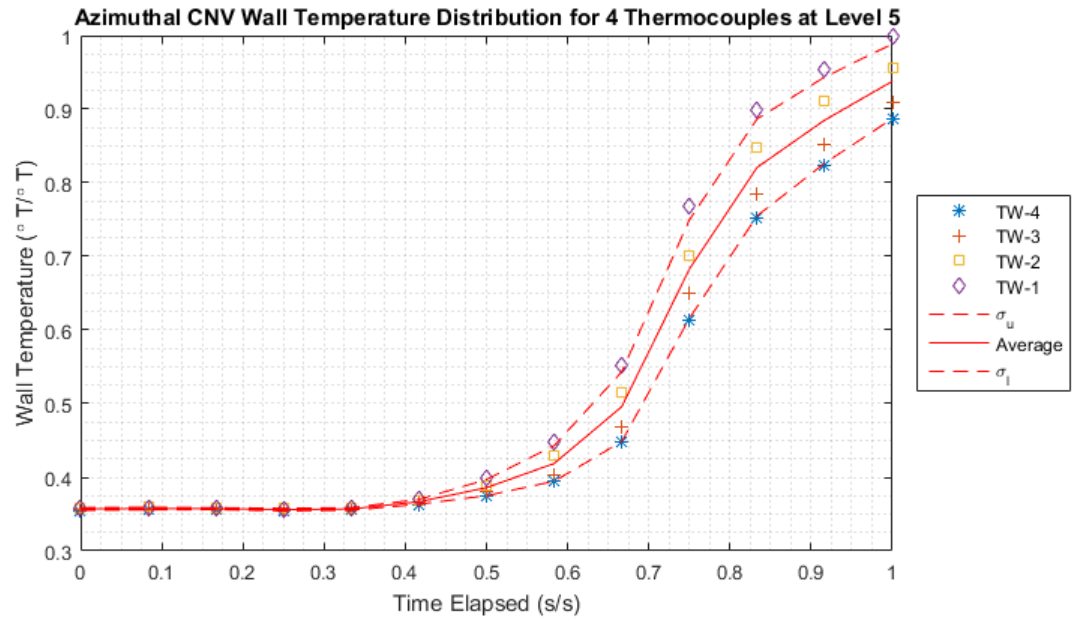
Figure 6.6: Temperature distribution in time for the four CNV TCs with the average and standard deviation values at level 5 (normalized in temperature and time).
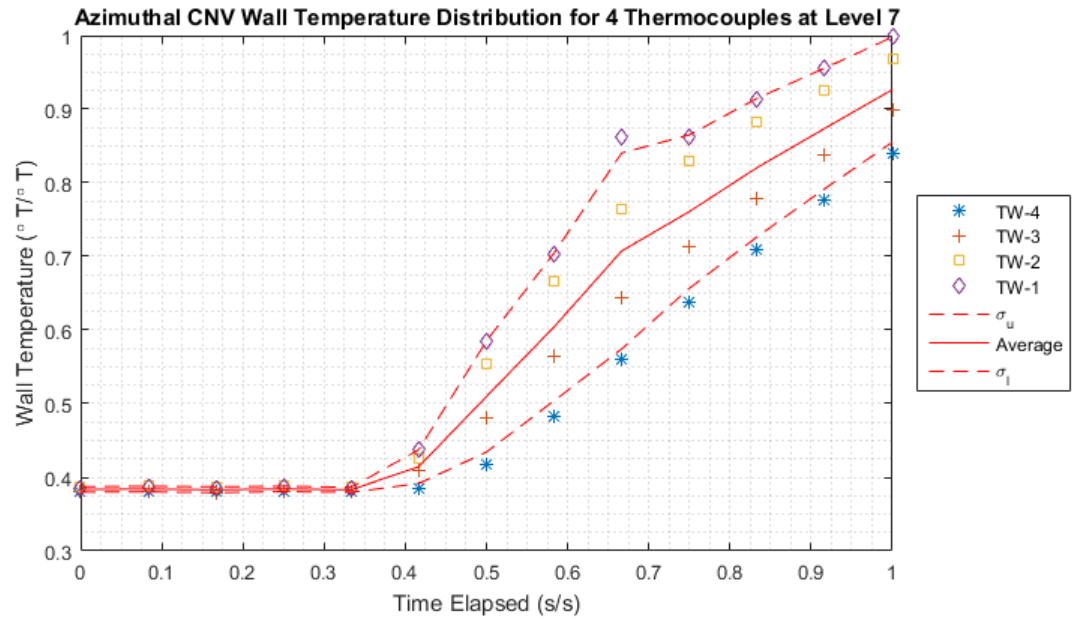
Figure 6.7: Temperature distribution in time for the four CNV TCs with the average and standard deviation values at level 7 (normalized in temperature and time).
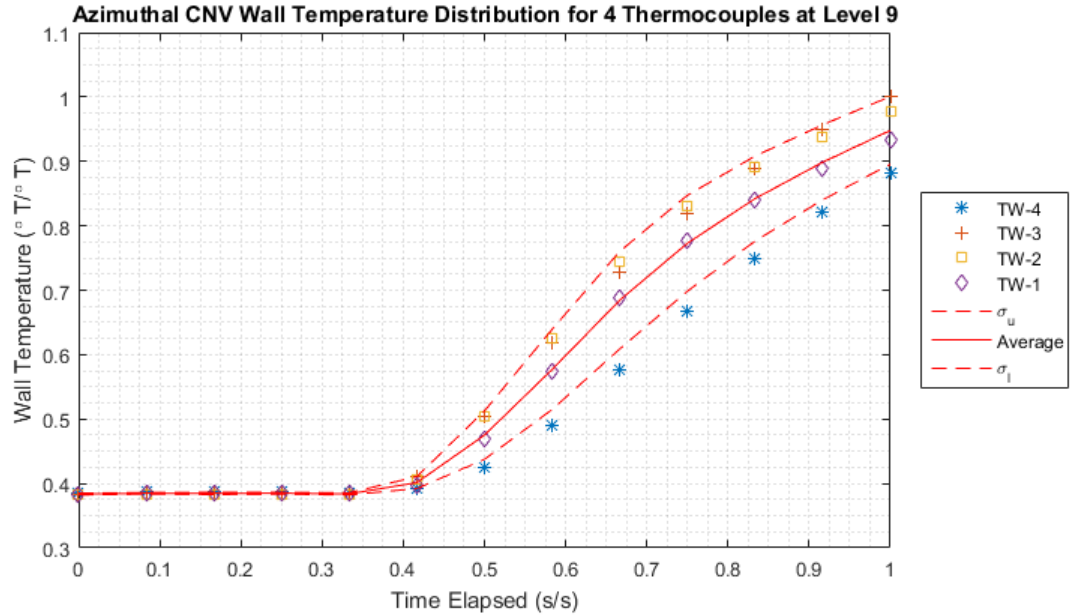
Figure 6.8: Temperature distribution in time for the four CNV TCs with the average and standard deviation values at level 9 (normalized in temperature and time).

With these figures in mind, initially most TCs are isothermal (the outliers are not supposed to exist since the HP-16b procedure requires the CNV wall temperatures to be pre-heated to spatially isothermal wall temperatures and is due to inefficient wall strip heaters). When proceeding in time as steam is injected and condensation starting to build on the inner wall, the temperatures begin to show distributions that are non-isothermal with large standard deviations up to 10% of the average value. Although in level 1 and 3, the standard deviations maintained to be minimal, levels 5, 7, and 9 are otherwise. Making the boundary condition an averaged value throughout the azimuthal distribution for the CNV inner wall is only valid at limited time frames and will create distortions within the simulation as the boundary condition is a forced Dirichlet boundary condition.

The boundary condition for the HTP on the non-CNV surface is made adiabatic since it is insulated with silicon with no water in the CPV. On HTP surface on the CNV side, adiabatic conditions were set as well. Considering that steam and condensation are potentially exposing the HTP wall, it would be invalid to do this if this were a validation simulation. When pondering on the types of heat transfer the HTP surface is experiencing, it is complicated to set heat flux wall conditions to keep the simulation true. With this simulation being an approximation and the fact that it is complex to calculate what the surface is truly experiencing, the adiabatic condition was set with full awareness this will add uncertainty to the simulation.

The last boundary condition is at the outer insulation surface where ambient environmental natural convection conditions were set.

6.4.5   Initial Condition Setup

The imported data described in section 6.4.4 is also used for initial conditions. Since the imported data includes time, the first data point of each known position is regarded as the initial condition. For locations such as the HTP and insulation where boundary conditions were not set, known temperatures from experimental test parameter were used. In the case of the HTP all heights were set at a single temperature value indicating azimuthal and lateral isothermal initial conditions. The following figure is the lateral HTP temperature distribution:
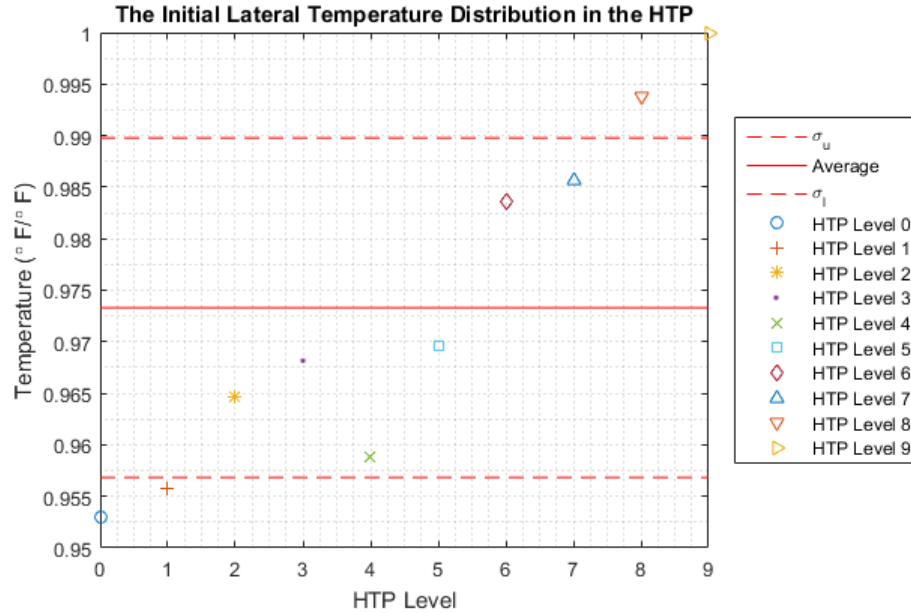
Figure 6.9: The lateral HTP initial temperature distribution (normalized in temperature). The x-axis just shows the level at uniform spacing.

Considering the height of the HTP to be several meters high, this lateral temperature distribution can be considered initially isothermal with small error.

6.5   Source of Errors

In an ideal CFD simulation, the generated data will agree with experimental throughout the whole transient with a relative and absolute error of zero. However with every approximation and assumption made, the simulated data is easily shifted from the true experimental data. The following sections describe the potential sources of error that is associated with this simulation.

6.5.1   Geometric Discrepancy

As mentioned in section 6.1.4, various external attachments to the CNV were not added to the geometry made in SOLIDWORKS. There are possibilities that some of the heat in the CNV was transferred and completely lost to the ambient air. If the amount of heat loss is significant, the simulation may overpredict the amount of heat transferred to the insulation resulting higher temperatures.

6.5.2   Meshing Error

By meshing the volume, finite number of cells are created to calculate the governing equations defined when physical models were chosen. Since the volume is divided into smaller cells, the act of meshing itself will contain a certain degree of error when considering the original geometry to be a continuous entity. If the mesh is large, the distribution of the quantity will be altered and the number of data points per length will be coarse. Such coarse meshes may lead to solution convergence issues. Typically, using small meshes are ideal and detailed distributions can be observed minimizing the error. Also depending on the type of the mesh, the geometry may be deformed to the point where the difference between the modeled geometry and the meshed geometry creates unintended distortions in data. The subdivided volume may also not fit well at interfaces between other structures with different mesh sizes which could result in creating a void and/or overlapping of meshes.

6.5.3   Discretization

To solve for the geometric volume, energy equations are discretized to make the problem solvable. In the simulation second-order scheme was chosen to ensure high accuracy in the energy equation (temporal scheme is first order) without sacrificing

extra computational power. If in the occasion that higher order terms are more influential than anticipated, the simulated data may unnecessarily distort from the experimental data. Another possibility is the scheme may not be well compatible with the given simulation. For example, central differencing schemes are good with diffusing problems but not when source terms exist or when the transport of some quantity is direction dependent. Since the specific scheme is not given in the manual or brochure, there is no telling what kind of scheme was used to fully analyze potential errors.

6.5.4   Physical Model Error

The final source of error roots from what physical models were selected. Unfortunately, every phenomena cannot be expressed into one unified model and assumptions combined with specialized theories must be applied to correctly model a single phenomenon. This optimization will always lead to some degree of error but minimized since it was made for that exact process. Therefore, it becomes crucial to select the correct model for the given situation. A good example of failure to chose correctly would be to use laminar flow models for turbulent flows. Even if the most applicable model was selected from the given lists of models provided from the CFD program, the model will have limitations where the minimized error is increased and there is no guarantee it will simulate all containing phenomena. To minimize error, it may be recommended to conduct trial and error to seek the best fitting model combination.

Chapter 7: Results

Before going onto the results and showing plots of temperature distributions, the convergence criteria and the proof of spatial and temporal grid convergence must be provided.

7.1 Convergence Criteria

The standard convergence criteria for a single quantity is less than 10^{-6} in error. Although the stopping criteria in STAR CCM+ is the limit to how many iterations will be run, it can be stopped manually at any moment to alter relaxation parameters to adjust the convergence to desired levels. Using this method, the error is less than 10^{-6} at any given point in the simulation.

7.2 CFD Grid Convergence

To ensure grid convergence a few steps is completed to determine the order of accuracy and the discretization error.

First, the average grid size in length is estimated with the following equation (from [27]):

$$h_s = \left[\frac{1}{N_c} \sum_{i=1}^{N_c} (\Delta V) \right]^{1/3} \tag{7.1}$$

Where h_s is the average grid size, N_c being the total number, and V as volume. Then the next parameter to calculate for is the grid refinement factor which is the

grid size ratio between two different grid sizes.

$$r = \frac{h_{s2}}{h_{s1}} \tag{7.2}$$

Where r is the Grid Refinement Factor (GRF) and h_{s2}/h_{s1} are grid sizes ($h_{s2} > h_{s1}$). Three spatial grid sizes were tested to achieve grid convergence. With known information from STAR CCM+, Table 7.1 shows the summary of grid sizes for all three spatial grid sizes.

Mesh Type	Coarse	Medium	Fine
Entire Volume (m^3)	0.7593	0.7593	0.7593
Number of Cells	3425	11285	13519
Grid Size (m)	0.06052	0.04067	0.03830

Table 7.1: Summary of grid size

The GRF from coarse to medium is 1.488 and from medium to fine is 1.0621. The same thing can be done for temporal grid by recognizing volume as the total time and number of cells as total number of time steps without the cube root. However it is doubtful this version would be used since the time step size is one of the primary parameters that are defined before any transient simulation. Similar to the spatial grid, three temporal grid sizes were selected to achieve temporal grid convergence. Due to the NDA between the author and NuScale Power, details of time step sizes are concealed to prevent the possibility of reverse engineering. The GRF however is reportable and is maintained to be 5 for both between coarse time and medium time, and medium time and fine time.

Typically a GRF of greater than 1.3 is recommended [27]. As reported in the paragraph above, the spatial grid refinement between medium and fine was only 1.0621. Although this was overlooked by the author and noticed only after post processing, the relative error between medium and coarse spatial grids were at

average 0.144%. This is small considering the GRF is 1.488 and it can be argued that the coarse spatial grid was already at high levels of accuracy thus possibly not requiring extra refinement.

After calculating the grid size and GRF, the order of accuracy can be calculated using the following four equations [27].

$$p = \frac{1}{\ln(r_{12})} \left| \ln \left| \frac{\epsilon_{32}}{\epsilon_{21}} \right| + q(p) \right| \tag{7.3}$$

$$q(p) = \ln \left(\frac{r_{21}^p - s}{r_{32}^p - s} \right) \tag{7.4}$$

$$s = 1 \cdot \text{sign} \left(\frac{\epsilon_{32}}{\epsilon_{21}} \right) \tag{7.5}$$

$$\epsilon_{ij} = \phi_i - \phi_j \tag{7.6}$$

Where i and j are representing two different grid sizes (1<2<3) and ϕ being the data point. The p in Eq. 7.3 and 7.4 is the order of accuracy. The order of accuracy is the truncation error in the given scheme where the relationship between grid size and accuracy in 1st order is linear, quadratic in 2nd order, cubic in 3rd order, and so on. By solving the equations iteratively, p can be determined with the exception of diverging parameters. To prevent non-converging p values, it is customary to make the GRF for both ratios to be the same so q in Eq. 7.5 is zero and Eq. 7.4 can be solved directly. As a caution, if ϵ_{ij} is extremely small, this method of calculating the order of accuracy can no longer be applied since it could potentially diverge or yield results that are unrealistic. The theoretical order of accuracy of space is 2nd order and time is 1st order (the author well aware that it is CFD industry standard for at least 2nd order to be maintained. Initially time was set as second order, due to mixing up old and new simulation settings, the time theoretical accuracy defaulted back to 1st order and this change was unnoticed until post processing).

The order of accuracy for space for CNV and HTP temperatures are given in Table 7.2.

Time (s)	CNV 1	CNV 3	CNV 5	CNV 7	HTP 1
5	0.9527	0.2025	0.1846	1.3338	11.1128
10	1.1228	0.2514	0.2224	1.3243	10.1930
15	1.2947	0.3316	0.2566	1.3090	9.6638
20	1.4690	0.1967	0.2849	1.2848	9.2975
25	1.6466	0.2825	0.3089	1.2651	9.0228
30	1.8287	0.3155	0.3306	1.2754	8.8079
35	2.0171	0.3410	0.3513	1.3258	8.6361
40	2.2142	0.3586	0.3711	1.4042	8.4974
45	2.4234	0.3669	0.3902	1.4717	8.3856
50	2.6498	0.3747	0.4088	1.5100	8.2967
55	2.9012	0.3874	0.4263	1.5241	8.2279
60	3.1897	0.4040	0.4422	1.5225	8.1773
65	3.5360	0.4216	0.4564	1.5099	8.1438
70	3.9773	0.4386	0.4695	1.4889	8.1267
75	4.5891	0.4527	0.4818	1.4612	8.1258
80	5.5524	0.4637	0.4937	1.4335	8.1411
85	7.4521	0.4746	0.5055	1.4216	8.1274
90	14.2728	0.4876	0.5173	1.4382	8.0879
95	0.4168	0.5031	0.5290	1.4842	8.0557
100	3.5111	0.5195	0.5400	1.5387	8.0302

Table 7.2: CNV wall temperature spatial grid order of accuracy for the first 100 seconds (the number s in the header row indicate height level). CNV Level 9, HTP Level 3, HTP Level 5, HTP Level 7, and HTP Level 9 spatial order of accuracy was either unable to calculate or unrealistic and was excluded from the grid convergence

The first 100 seconds in 5 second increments are only shown as a preview. To show the whole data set would take multiple pages to show and is unnecessary. First, only CNV Levels 1, 3, 5, 7 are shown. This is due to the fact that CNV level 9 order of accuracy and all of HTP order of accuracy in space were either unable to calculate or the value was unrealistic to present. As mentioned earlier, if ϵ_{ij} is small to a certain degree the analysis above cannot apply. The global order of accuracy of CNV level 1, CNV level 3, CNV level 5, CNV level 7, and HTP level 1 over the whole time is 2.6, 0.6165, 0.6480, 1.4747, and 7.3613 with an average of 2.5436. Considering the theoretical accuracy being 2nd order accurate, it is reasonable for the global average order of accuracy to be around the theoretical order of accuracy. To account for the order of accuracy at locations where the calculation method did not match, showing the relative error distribution can reveal whether oscillations are taking place. The following plot is an example of how the relative error for the coarse, medium, and fine data compared to the actual value is:
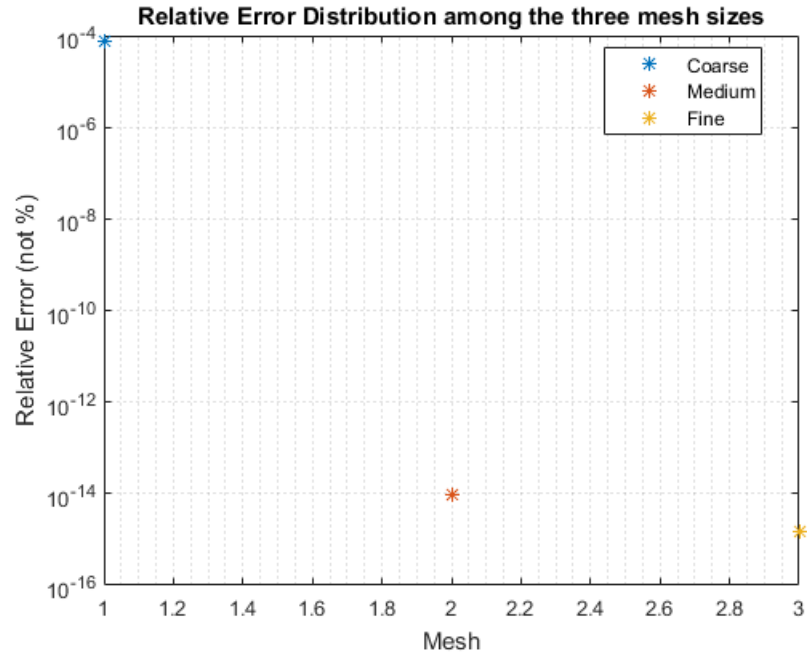
Figure 7.1: Distribution of relative error comparing values at different spatial mesh sizes with actual value. The x-axis does not represent anything and is there to provide equal spacing between data points.

Figure 7.1 actually represents all the data generated by the simulation. No relative error shows indication of either medium or fine relative error being larger than the coarse (even in the case of fine being larger than medium) which implies no oscillations within the grid convergence. Another thing to note is that the relative error is decreasing quadratically which is one of the traits of 2nd order accuracy.

For the time grid order of accuracy, the relative error was moderately small yielding the following results in Tables 7.3 and 7.4.

Time (s)	CNV 1	CNV 3	CNV 5	CNV 7	CNV 9
5	0.9463	0.9464	0.9480	0.9500	0.9473
10	0.9496	0.9492	0.9510	0.9528	0.9503
15	0.9529	0.9519	0.9539	0.9556	0.9533
20	0.9562	0.9547	0.9568	0.9584	0.9563
25	0.9595	0.9575	0.9598	0.9611	0.9594
30	0.9628	0.9604	0.9627	0.9638	0.9624
35	0.9660	0.9633	0.9657	0.9666	0.9654
40	0.9693	0.9662	0.9686	0.9694	0.9685
45	0.9725	0.9692	0.9716	0.9722	0.9715
50	0.9756	0.9722	0.9745	0.9748	0.9745
55	0.9788	0.9754	0.9775	0.9775	0.9776
60	0.9819	0.9785	0.9804	0.9801	0.9806
65	0.9849	0.9818	0.9832	0.9828	0.9837
70	0.9879	0.9853	0.9861	0.9855	0.9868
75	0.9909	0.9887	0.9888	0.9882	0.9899
80	0.9938	0.9924	0.9915	0.9906	0.9929
85	0.9967	0.9963	0.9940	0.9931	0.9960
90	0.9994	1.0003	0.9964	0.9956	0.9990
95	1.0021	1.0046	0.9987	0.9981	1.0021
100	1.0048	1.0091	1.0008	1.0005	1.0052

Table 7.3: CNV wall temperature time grid order of accuracy for the first 100 seconds (the number s in the header row indicate height level).

Time (s)	HTP 1	HTP 3	HTP 5	HTP 7	HTP 9
5	0.9703	0.9754	0.9826	0.9782	0.9788
10	0.9729	0.9763	0.9789	0.9787	0.9792
15	0.9745	0.9764	0.9793	0.9791	0.9797
20	0.9756	0.9754	0.9797	0.9796	0.9802
25	0.9765	0.9775	0.9802	0.9800	0.9806
30	0.9773	0.9700	0.9807	0.9805	0.9811
35	0.9780	0.9773	0.9811	0.9810	0.9816
40	0.9786	0.9777	0.9816	0.9814	0.9820
45	0.9791	0.9770	0.9820	0.9819	0.9825
50	0.9797	0.9764	0.9825	0.9823	0.9829
55	0.9802	0.9778	0.9830	0.9828	0.9834
60	0.9808	0.9773	0.9834	0.9833	0.9839
65	0.9813	0.9869	0.9839	0.9837	0.9843
70	0.9818	0.9811	0.9844	0.9842	0.9848
75	0.9823	0.9839	0.9838	0.9847	0.9852
80	0.9828	0.9845	0.9853	0.9851	0.9857
85	0.9833	0.9961	0.9858	0.9856	0.9861
90	0.9838	0.9840	0.9862	0.9860	0.9866
95	0.9843	0.9848	0.9867	0.9865	0.9870
100	0.9848	0.9831	0.9872	0.9870	0.9875

Table 7.4: HTP wall temperature time grid order of accuracy for the first 100 seconds (the number s in the header row indicate height level).

The order of accuracy for time was reasonable compared to the set 1st order accuracy and since no iterative procedure was required (the GRF was maintained to be the same), abnormal order of accuracies were not observed. The global average order of accuracy is 1.0014 which implies there was minimal loss of accuracy compared to the theoretical order of accuracy. Similar to the spatial grid, the plot of relative error can be provided as the following figure:
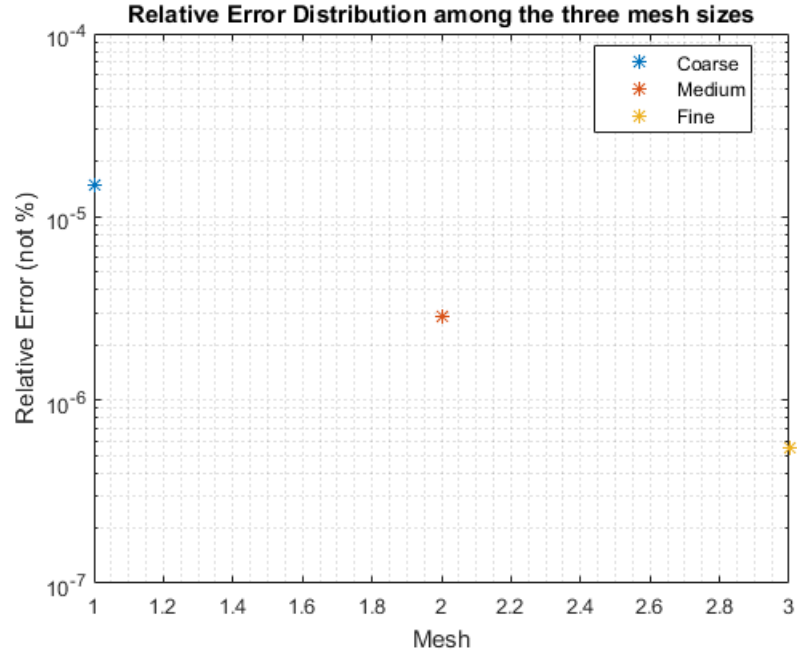
Figure 7.2: Distribution of relative error comparing values at different temporal mesh sizes with actual value. The x-axis does not represent anything and is there to provide equal spacing between data points.

Figure 7.2 represents all time relative error distributions where no oscillations were observed. Since the order of accuracy is 1st order, it explains why as the time mesh is smaller the relative error becomes smaller as well linearly.

The GCI method uses the approximate relative error and p to solve for the fine-grid convergence index which is a measure of grid convergence. If the GCI is smaller than the accuracy required, it is typically a good measure of grid convergence. The following are the equations used:

Approximate Relative Error:

$$e_a^{21} = \left| \frac{\phi_1 - \phi_2}{\phi_1} \right| \tag{7.7}$$

Fine-Grid Convergence Index:

$$GCI_{fine}^{21} = \frac{1.25 e_a^{21}}{r_{21}^p - 1} \tag{7.8}$$

Using the parameters in from Tables 7.2, 7.3, and 7.4, the GRF, and generated data points, the following tables are the first 100 seconds of CNV and HTP wall temperature spatial and temporal fine-grid convergence index values.

Time (s)	CNV 1	CNV 3	CNV 5	CNV 7	HTP 1
5	8.2472e-05	2.5520e-06	1.4401e-05	1.9336e-07	1.1550e-05
10	1.4589e-04	2.8429e-06	2.9693e-05	3.8315e-07	2.4678e-05
15	1.9345e-04	1.4213e-06	4.5342e-05	5.6872e-07	3.7619e-05
20	2.2785e-04	1.2541e-06	6.0890e-05	7.5156e-07	4.9818e-05
25	2.5138e-04	4.7936e-06	7.6014e-05	9.2545e-07	6.0980e-05
30	2.6596e-04	8.8958e-06	9.0519e-05	1.0706e-06	7.0929e-05
35	2.7326e-04	1.3323e-05	1.0428e-04	1.1715e-06	7.9555e-05
40	2.7470e-04	1.7866e-05	1.1720e-04	1.2317e-06	8.6792e-05
45	2.7151e-04	2.2349e-05	1.2924e-04	1.2817e-06	9.2607e-05
50	2.6481e-04	2.6701e-05	1.4039e-04	1.3400e-06	9.6989e-05
55	2.5564e-04	3.0893e-05	1.5064e-04	1.4066e-06	9.9949e-05
60	2.4505e-04	3.4884e-05	1.5997e-04	1.4778e-06	1.0151e-04
65	2.3429e-04	3.8624e-05	1.6842e-04	1.5516e-06	1.0172e-04
70	2.2519e-04	4.2079e-05	1.7604e-04	1.6272e-06	1.0062e-04
75	2.2146e-04	4.5215e-05	1.8291e-04	1.7046e-06	9.8269e-05
80	2.3413e-04	4.8021e-05	1.8909e-04	1.7775e-06	9.4748e-05
85	3.2951e-04	5.0539e-05	1.9465e-04	1.8281e-06	9.3954e-05
90	4.2894e-04	5.2816e-05	1.9965e-04	1.8405e-06	9.5517e-05
95	3.5260e-04	5.4877e-05	2.0413e-04	1.8138e-06	9.6642e-05
100	4.5776e-06	5.6717e-05	2.0812e-04	1.7735e-06	9.7347e-05

Table 7.5: CNV and HTP wall temperature spatial grid GCI for the first 100 seconds (the number s in the header row indicate height level). GCI values of locations where a reasonable order of accuracy was attained are only shown.

Time (s)	CNV 1	CNV 3	CNV 5	CNV 7	CNV 9
5	1.8306e-05	1.6158e-05	2.1838e-05	2.0763e-05	2.5559e-05
10	3.1203e-05	2.7500e-05	3.7301e-05	3.5675e-05	4.3520e-05
15	3.9941e-05	3.5065e-05	4.7781e-05	4.5975e-05	5.5531e-05
20	4.5494e-05	3.9689e-05	5.4405e-05	5.2681e-05	6.2941e-05
25	4.8630e-05	4.2061e-05	5.8093e-05	5.6578e-05	6.6842e-05
30	4.9952e-05	4.2741e-05	5.9580e-05	5.8314e-05	6.8111e-05
35	4.9934e-05	4.2176e-05	5.9440e-05	5.8446e-05	6.7457e-05
40	4.8944e-05	4.0711e-05	5.8134e-05	5.7416e-05	6.5436e-05
45	4.7271e-05	3.8622e-05	5.6025e-05	5.5568e-05	6.2471e-05
50	4.5138e-05	3.6134e-05	5.3396e-05	5.3165e-05	5.8893e-05
55	4.2714e-05	3.3421e-05	5.0456e-05	5.0351e-05	5.4953e-05
60	4.0131e-05	3.0598e-05	4.7365e-05	4.7305e-05	5.0844e-05
65	3.7485e-05	2.7762e-05	4.4243e-05	4.4169e-05	4.6708e-05
70	3.4848e-05	2.4992e-05	4.1182e-05	4.1043e-05	4.2662e-05
75	3.2272e-05	2.2329e-05	3.8238e-05	3.8001e-05	3.8774e-05
80	2.9792e-05	1.9806e-05	3.5451e-05	3.5055e-05	3.5088e-05
85	2.7434e-05	1.7451e-05	3.2848e-05	3.2214e-05	3.1629e-05
90	2.5212e-05	1.5284e-05	3.0442e-05	2.9522e-05	2.8412e-05
95	2.3133e-05	1.3302e-05	2.8233e-05	2.7006e-05	2.5442e-05
100	2.1201e-05	1.1499e-05	2.6220e-05	2.4681e-05	2.2724e-05

Table 7.6: CNV wall temperature time grid GCI for the first 100 seconds (the numbers in the header row indicate height level).

Time (s)	HTP 1	HTP 3	HTP 5	HTP 7	HTP 9
5	1.6600e-06	8.1796e-06	1.4014e-05	1.4493e-05	1.5650e-05
10	3.0445e-06	1.4792e-05	2.6478e-05	2.7281e-05	2.9503e-05
15	4.2288e-06	2.0998e-05	3.7387e-05	3.8503e-05	4.1698e-05
20	5.2439e-06	2.6955e-05	4.6896e-05	4.8283e-05	5.2363e-05
25	6.1101e-06	3.1388e-05	5.5124e-05	5.6672e-05	6.1622e-05
30	6.8431e-06	3.6114e-05	6.2181e-05	6.3896e-05	6.9590e-05
35	7.4566e-06	3.8919e-05	6.8170e-05	7.0013e-05	7.6379e-05
40	7.9624e-06	4.1865e-05	7.3191e-05	7.5119e-05	8.2093e-05
45	8.3715e-06	4.4947e-05	7.7332e-05	7.9310e-05	8.6829e-05
50	8.6935e-06	4.6697e-05	8.0680e-05	8.2672e-05	9.0675e-05
55	8.9376e-06	4.8631e-05	8.3313e-05	8.5289e-05	9.3718e-05
60	9.1118e-06	5.0310e-05	8.5305e-05	8.7246e-05	9.6040e-05
65	9.2238e-06	4.9704e-05	8.6727e-05	8.8616e-05	9.7716e-05
70	9.2805e-06	4.9729e-05	8.7644e-05	8.9461e-05	9.8817e-05
75	9.2883e-06	4.9750e-05	8.8304e-05	8.9837e-05	9.9402e-05
80	9.2529e-06	4.9363e-05	8.7955e-05	8.9806e-05	9.9531e-05
85	9.1798e-06	4.6778e-05	8.7677e-05	8.9294e-05	9.9258e-05
90	9.0738e-06	4.7488e-05	8.6677e-05	8.8568e-05	9.8633e-05
95	8.9394e-06	4.6810e-05	8.5807e-05	8.7561e-05	9.7700e-05
100	8.7807e-06	4.6274e-05	8.4698e-05	8.6313e-05	9.6502e-05

Table 7.7: HTP wall temperature time grid GCI for the first 100 seconds (the number s in the header row indicate height level).

As all previews are small and based on Figure 7.1 and Figure 7.2, partial spatial grid convergence and temporal grid convergence was achieved. For good measure the asymptotic range will also be investigated by using the following equation:

$$GCI_{32} = r^p GCI_{21} \text{ or } \frac{GCI_{32}}{r^p GCI_{21}} = 1 \tag{7.9}$$

When Eq. 7.9 is valid, the grid can be said to be within the asymptotic range and asymptotically converged. The following tables show the first 100 seconds of $\frac{GCI_{32}}{r^p GCI_{21}}$ ratio values:

Time (s)	CNV 1	CNV 3	CNV 5	CNV 7	HTP 1
5	0.4688	0.8514	0.8634	1	0.3305
10	0.4094	0.8189	0.8378	1	0.3081
15	0.3571	0.7683	0.8153	1	0.2954
20	0.3109	0.8552	0.7971	1	0.2867
25	0.2699	0.7988	0.7821	1	0.2802
30	0.2335	0.7782	0.7686	1	0.2752
35	0.2011	0.7625	0.7560	1	0.2712
40	0.1719	0.7519	0.7442	1	0.2681
45	0.1456	0.7470	0.7329	1	0.2655
50	0.1216	0.7423	0.7222	1	0.2635
55	0.09960	0.7349	0.7121	1	0.2619
60	0.07920	0.7252	0.7032	1	0.2608
65	0.06010	0.7151	0.6953	1	0.2600
70	0.04230	0.7055	0.6881	1	0.2596
75	0.02600	0.6976	0.6813	1	0.2596
80	0.01210	0.6916	0.6749	1	0.2599
85	0.002700	0.6856	0.6686	1	0.2596
90	1.1819e-05	0.6786	0.6623	1	0.2588
95	0.1518	0.6702	0.6562	1	0.2580
100	0.1746	0.6616	0.6505	1	0.2575

Table 7.8: The CNV and HTP spatial GCI ratio.

Time (s)	CNV 1	CNV 3	CNV 5	CNV 7	CNV 9
5	1.0001	1.0000	0.9999	0.9999	0.9999
10	1.0001	0.9999	0.9999	0.9999	0.9999
15	1.0001	0.9999	0.9999	0.9999	0.9998
20	1.0001	0.9999	0.9998	0.9998	0.9998
25	1.0001	0.9999	0.9998	0.9998	0.9998
30	1.0001	0.9999	0.9998	0.9998	0.9998
35	1.0001	0.9999	0.9998	0.9998	0.9998
40	1.0001	0.9999	0.9998	0.9998	0.9998
45	1.0001	0.9999	0.9998	0.9998	0.9998
50	1.0001	0.9999	0.9998	0.9998	0.9998
55	1.0001	0.9999	0.9998	0.9998	0.9998
60	1.0001	0.9999	0.9999	0.9999	0.9998
65	1.0001	0.9999	0.9999	0.9999	0.9999
70	1.0001	0.9999	0.9999	0.9999	0.9999
75	1.0001	0.9999	0.9999	0.9999	0.9999
80	1.0001	0.9999	0.9999	0.9999	0.9999
85	1.0001	0.9999	0.9999	0.9999	0.9999
90	1.0001	1.0000	0.9999	0.9999	0.9999
95	1.0001	1.0000	0.9999	0.9999	0.9999
100	1.0001	1.0000	0.9999	0.9999	0.9999

Table 7.9: The CNV time GCI ratio.

Time (s)	HTP 1	HTP 3	HTP 5	HTP 7	HTP 9
5	1.0000	1.0000	1.0000	1.0000	1.0000
10	1.0000	1.0000	0.9999	0.9999	0.9999
15	1.0000	0.9999	0.9999	0.9999	0.9999
20	1.0000	0.9999	0.9999	0.9999	0.9998
25	1.0000	0.9999	0.9998	0.9998	0.9998
30	1.0000	0.9999	0.9998	0.9998	0.9998
35	1.0000	0.9999	0.9998	0.9998	0.9998
40	1.0000	0.9999	0.9998	0.9998	0.9997
45	1.0000	0.9999	0.9998	0.9998	0.9997
50	1.0000	0.9999	0.9998	0.9997	0.9997
55	1.0000	0.9999	0.9997	0.9997	0.9997
60	1.0000	0.9998	0.9997	0.9997	0.9997
65	1.0000	0.9998	0.9997	0.9997	0.9997
70	1.0000	0.9998	0.9997	0.9997	0.9997
75	1.0000	0.9998	0.9997	0.9997	0.9997
80	1.0000	0.9998	0.9997	0.9997	0.9997
85	1.0000	0.9999	0.9997	0.9997	0.9997
90	1.0000	0.9999	0.9997	0.9997	0.9997
95	1.0000	0.9999	0.9997	0.9997	0.9997
100	1.0000	0.9999	0.9997	0.9997	0.9997

Table 7.10: The HTP time GCI ratio.

The spatial global average of space is 0.7480 and is quite far from 1. Locally, some locations were close to 1 and some were on the magnitude of 10^{-2}. Overall, the spatial grid is only partially within the asymptotic range. In terms of time, the global average is 0.9991 with most local values to be around 1 indicating all are within the asymptotic range. Note that not being within the asymptotic range does not imply bad grid convergence.

In total seven combinations of space and time grids were used. Out of the five were to arrive at an acceptable space and time grid size based on the generated data of each combination. Figure 7.3 illustrates the process taken to arrive at final space and time grid size.
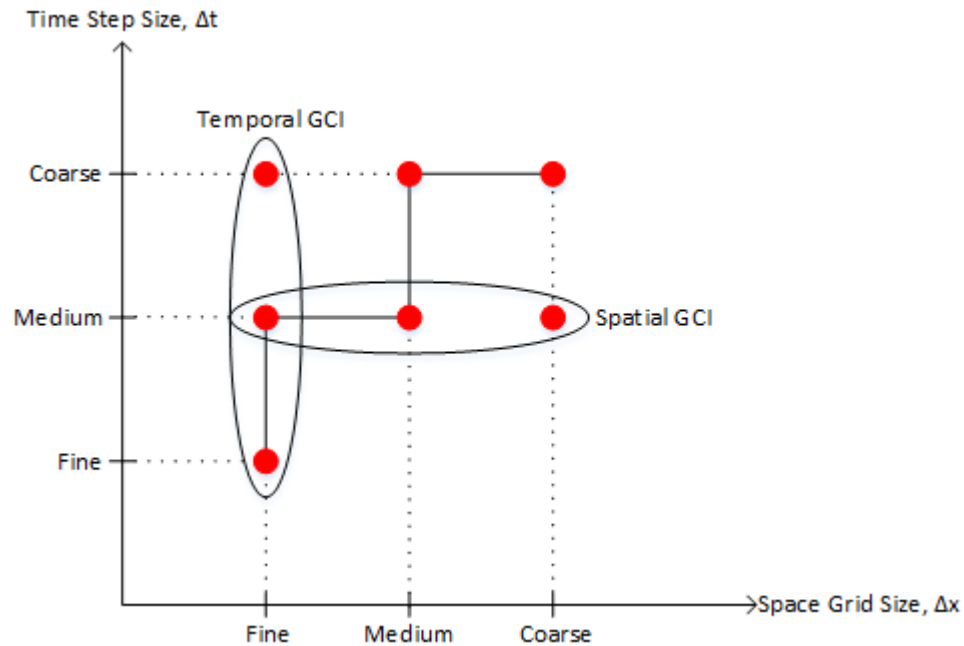

Figure 7.3: Grid convergence process for space and time (this plot is not to scale).

Starting from coarse space and time, the next simulation's grid size would either be refined in space and time. At the fifth simulation where fine space and time were achieved, the grid refinement process was suspended yielding well converged results. To conduct the GCI for space and time, two extra simulations were conducted at coarse time/fine space and medium time/coarse space. The main reason for this action is to conduct the GCI at a constant time or space grid while assessing grid convergence for the other grid type. It was convenient to select the two points because it would amount to the least number of total simulations. If the space GCI was applied at fine time, then two extra simulations would have to be run.

7.3 Generated Data

The following plots are the generated data with error bars when it is applicable. The errors will be based on the time error since it is orders larger than the space error. All values are given normalized, the time increment of each data point is not given, and the total time is not given to protect NuScale Power proprietary data.

7.3.1 CNV Wall Temperatures
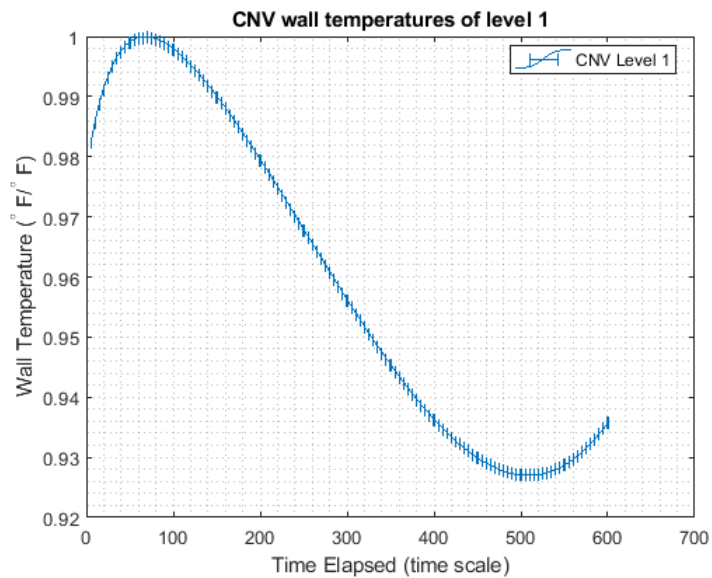
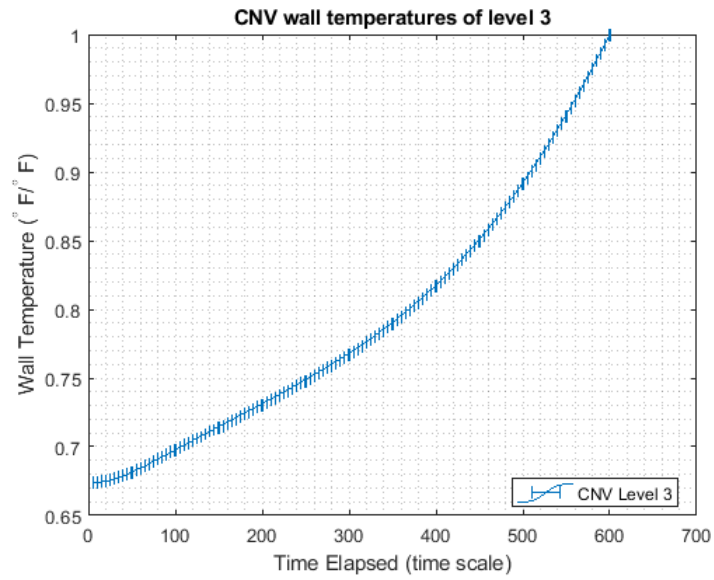Figure 7.4: CNV wall temperature at level 1 with error bars.
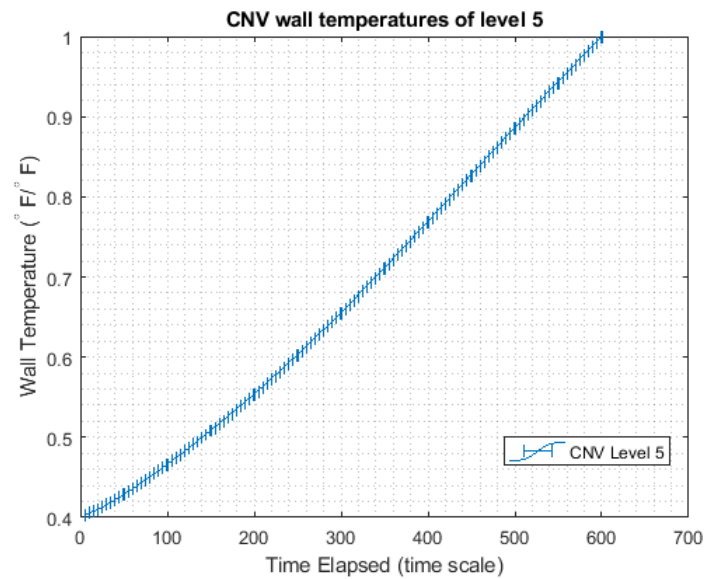
Figure 7.5: CNV wall temperature at level 3 with error bars.

Figure 7.6: CNV wall temperature at level 5 with error bars.
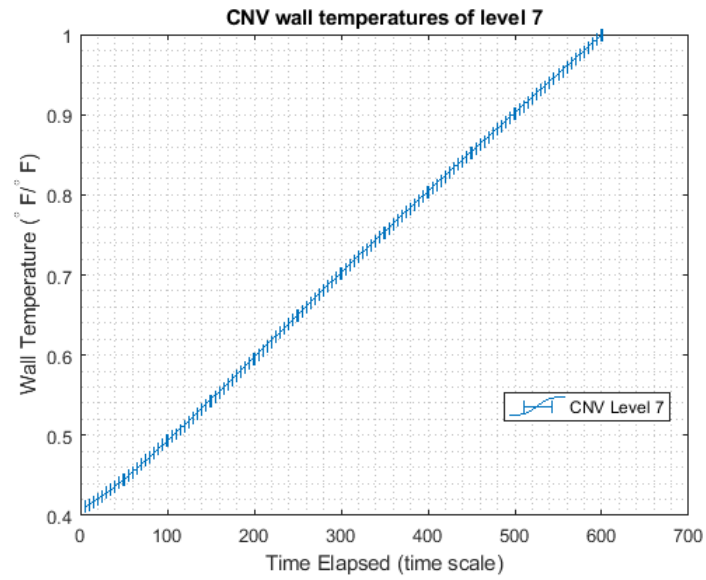
Figure 7.7: CNV wall temperature at level 7 with error bars.
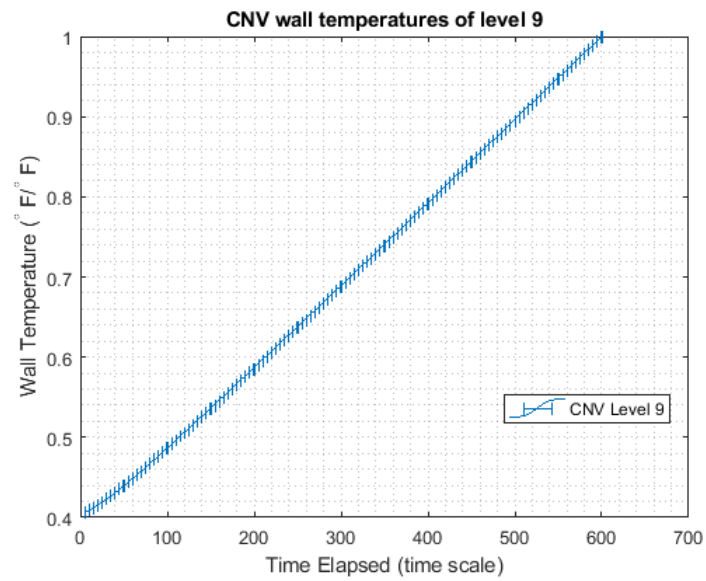
Figure 7.8: CNV wall temperature at level 1 with error bars.

7.3.2   HTP Wall Temperatures
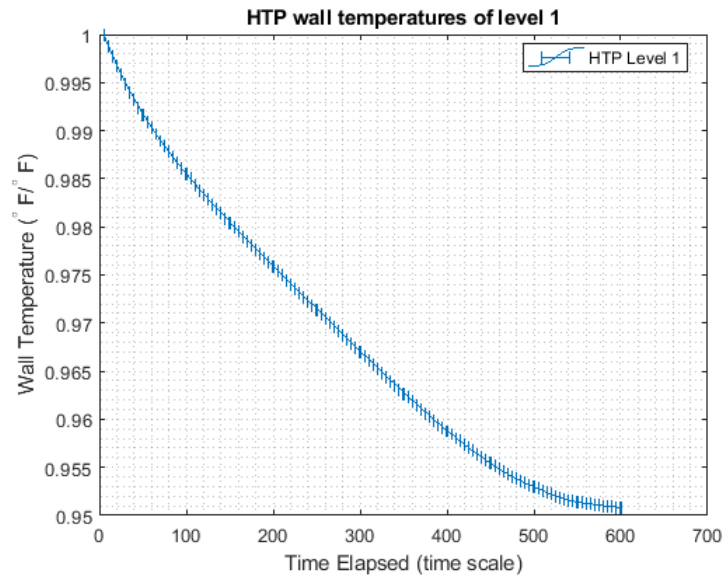
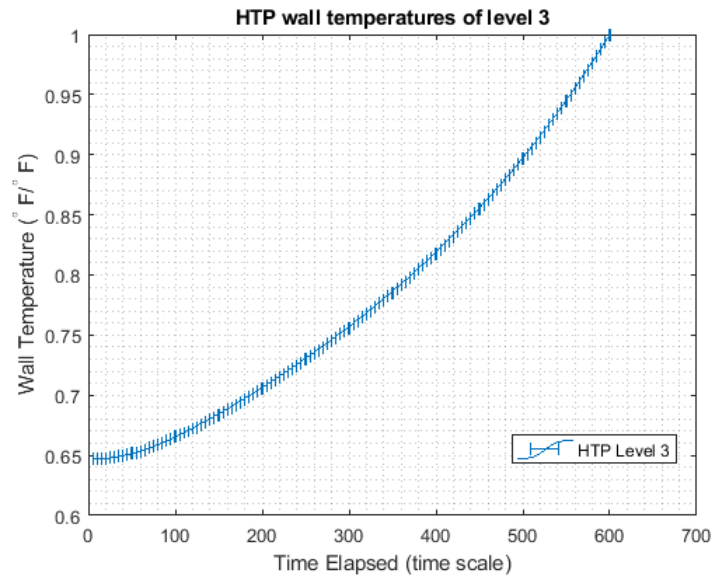
Figure 7.9: HTP wall temperature at level 1 with error bars.

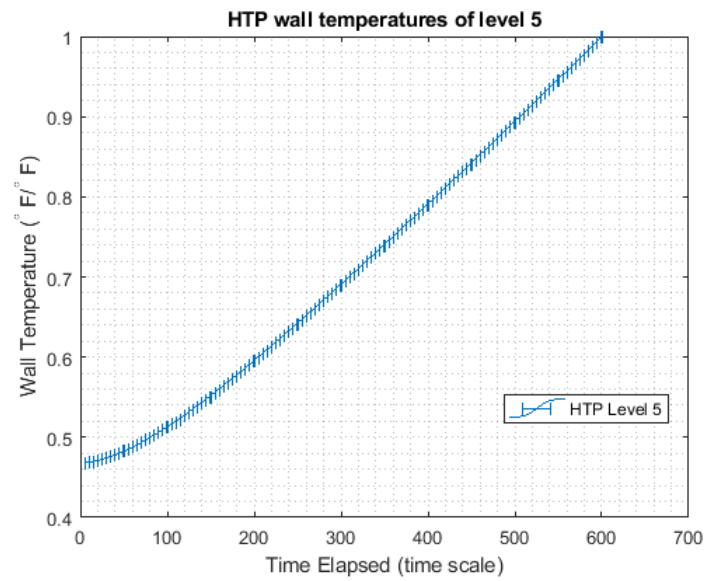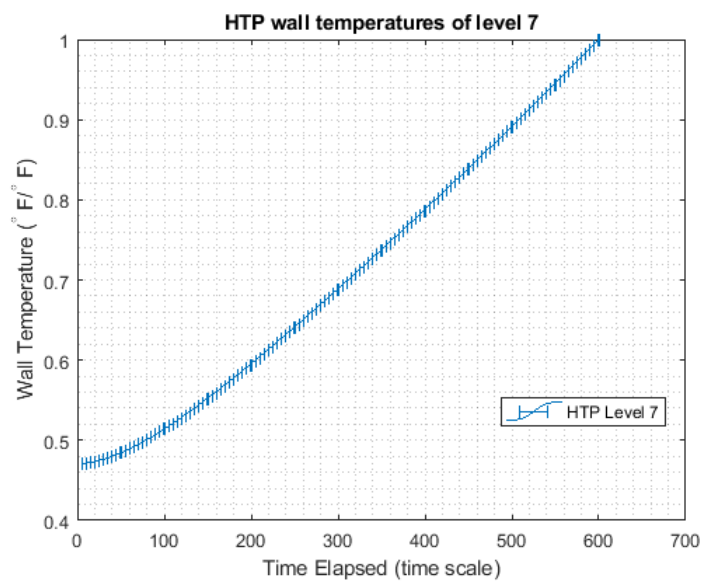Figure 7.10: HTP wall temperature at level 3 with error bars.

Figure 7.11: HTP wall temperature at level 5 with error bars.

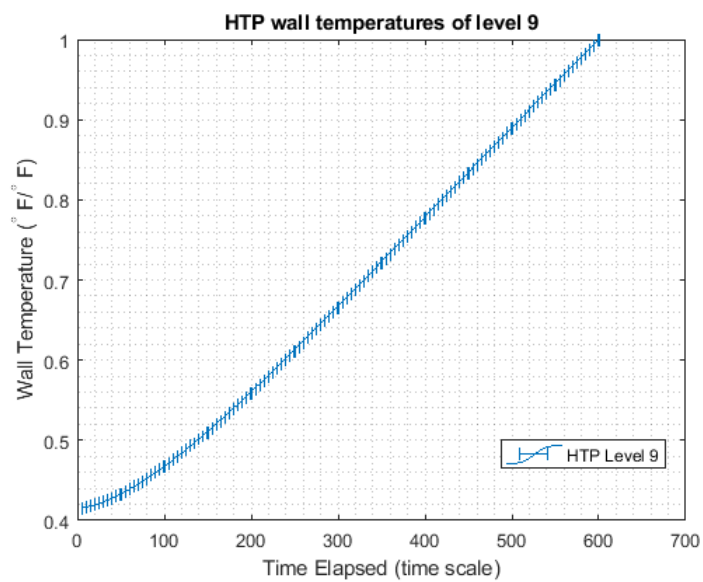Figure 7.12: HTP wall temperature at level 7 with error bars.

Figure 7.13: HTP wall temperature at level 9 with error bars.

7.3.3   Energy Residual and Insulation Outer Wall Heat Flux
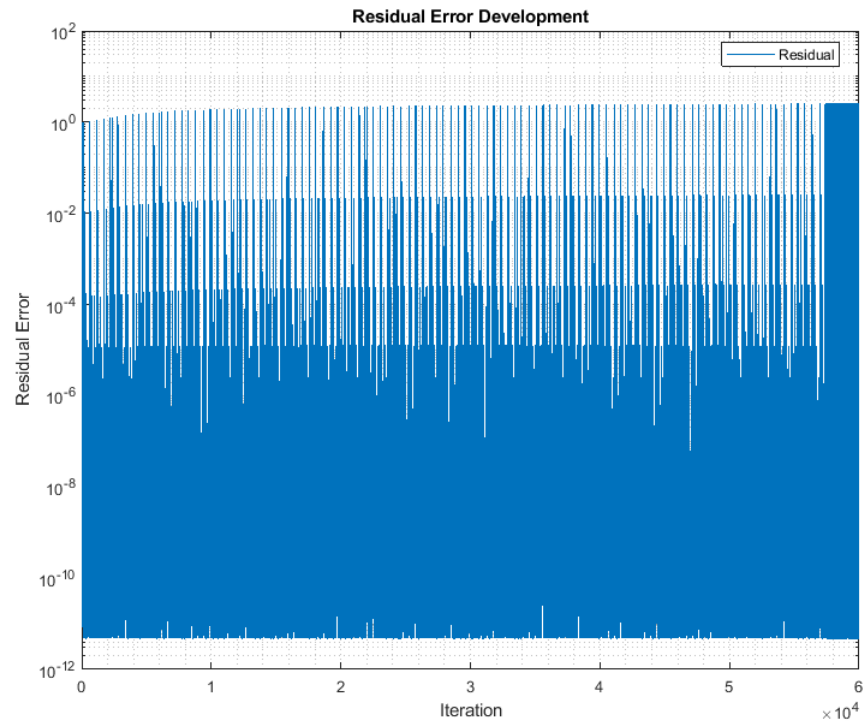

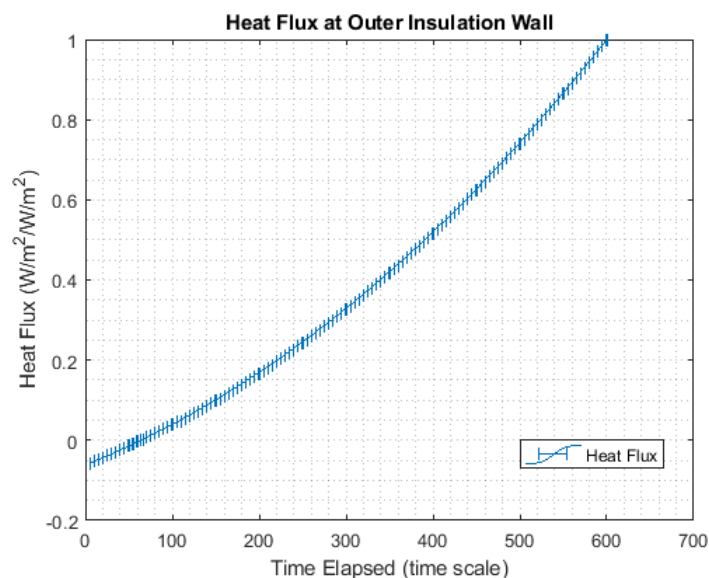Figure 7.14: The energy residual with error bars.

Figure 7.15: The Insulation outer wall heat flux with error bars.

7.4   Comparison of HTP Wall Temperatures

Since the boundary conditions were the inner wall CNV temperatures, the HTP midpoint wall temperature will be used to validate this simulation. As mentioned before, TH insertion depth is documented. Relative positions are given in the NIST-1 Piping and Instrumentation Diagram drawings making it possible to know whether a TC is north, south, east, and west of another TC. To determine which TC best matches the simulated data at the approximate simulated location, the TCs at the same level were cross-plotted with the simulated data to find which TC behaved similarly within the temperature range.

The following plots will be the HTP plate wall temperatures compared with simulated data at the same height. It should be mentioned that typical TCs have measurement uncertainties of about $\pm3.96°F$ (about $\pm2.2°C$). The TCs in NIST-1 are periodically verified to ensure the TCs read within the tolerance that NIST-1

upholds. With this in mind, the TC readings will be regarded to have the standard uncertainty of $\pm 3.96°$F.
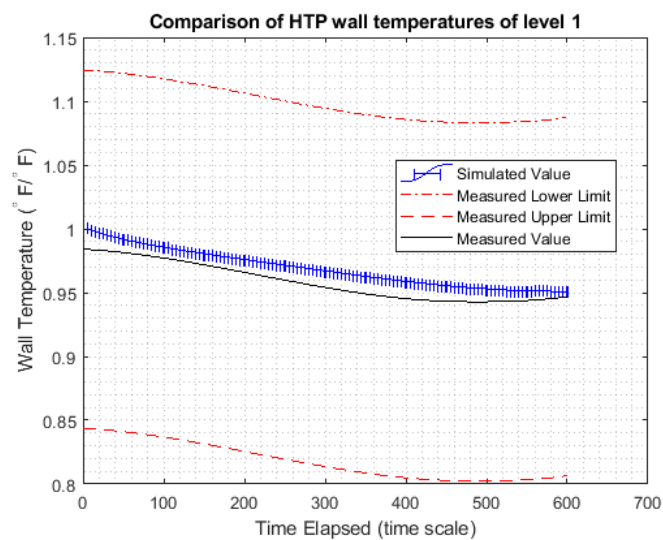

Figure 7.16: Data comparison between experimental and simulated HTP wall temperatures at level 1 with error bars.

Figure 7.17: Data comparison between experimental and simulated HTP wall temperatures at level 3 with error bars.

Figure 7.18: Data comparison between experimental and simulated HTP wall temperatures at level 5 with error bars.
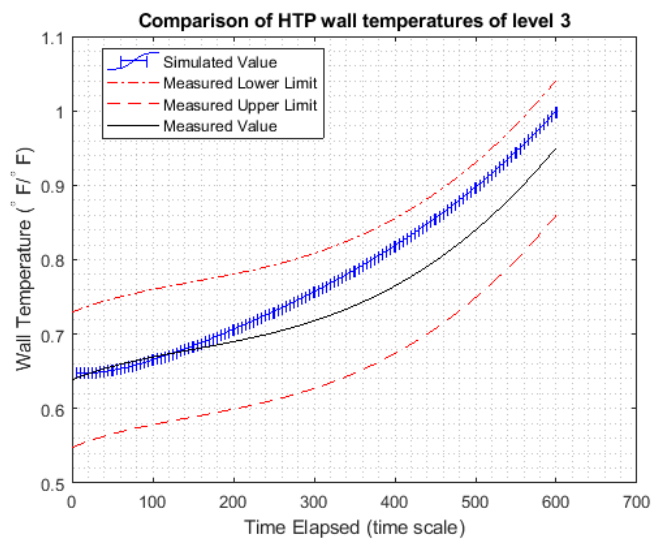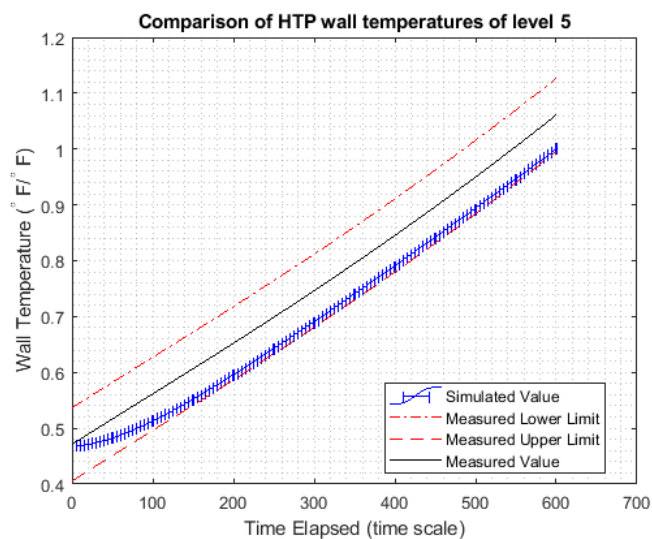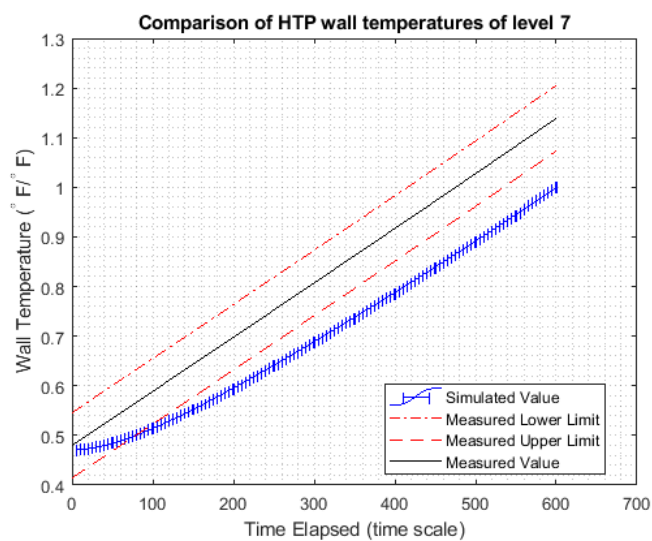
Figure 7.19: Data comparison between experimental and simulated HTP wall temperatures at level 7 with error bars.
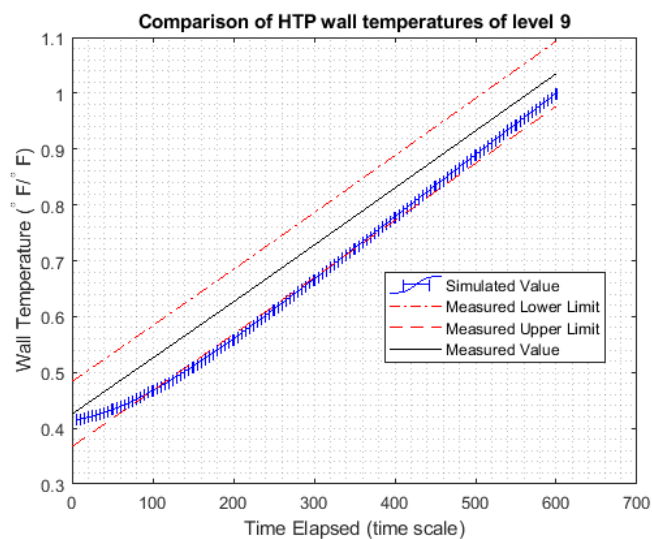

Figure 7.20: Data comparison between experimental and simulated HTP wall temperatures at level 9 with error bars.

As what can be observed with Figures 7.16, 7.17, 7.18, 7.19, and 7.20, some simulated data portions fit within the TC uncertainty tolerance with the errors bars included and some do not. In terms of trends, most of the simulated follow the experimented data. Considering the boundary condition locations are at separate locations than the HTP, it is surprising how the simulated data can agree to this degree with the experimental data. The following figure shows the geometric locations of the inner CNV wall and HTP midpoint wall from a birds eye view.
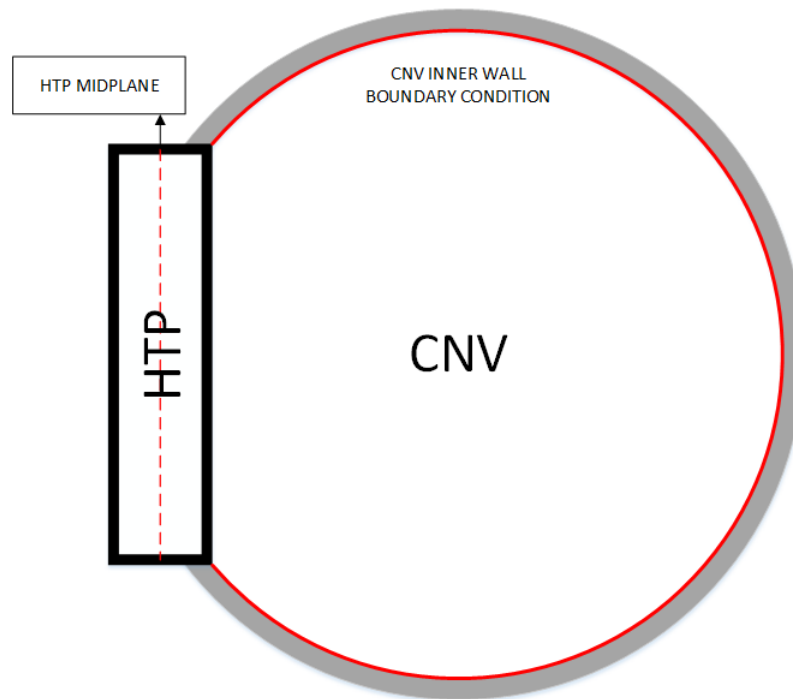

Figure 7.21: Simplistic Bird View of the CNV and HTP.

The simulation can be considered mostly validated with the exception of level 7 HTP wall temperatures.

Chapter 8: Conclusion

When observing the comparison done in section 7.4, the agreement with experimental data is good with the exception of level 7 deviating more than other levels. Visualizing the internal volume of the CNV, superheated steam is continuously experiencing phase change to liquid water while accumulating at the bottom of the CNV. As the test progresses, the water level of the CNV increases until it is eventually drained. Levels 3, 5, and 7 are more located to the middle section of the CNV where it may be submerged or still has exposure to superheated steam. On the other hand, levels 1 and 9 are mostly exposed to the same fluid throughout the test (level 1 being submerged in water and level 9 exposed to superheated steam). This inconsistency in which phase dominates at different levels at different times could be the main contributor to the less accurate simulation at mid-section levels. Another possibility is to consider the case of insufficient number of known data points. As mentioned in section 6.4.2, the CNV boundary conditions are given for finite number of points where automatic interpolation and extrapolation is conducted by STAR CCM+ to account for locations and time with no exact data input. The interpolation or extrapolation operations tend to project smooth temperature distributions for the given interval. The condensation, forced convection, and conduction combination in the CNV may not always provide smooth temperature distributions and potentially can have hot or cold spots which may seem as outliers in the scheme of data. There may be numerous high differential temperature per length (or per time) data points that STAR CCM+ cannot anticipate. If the simulation were to be shifted back to point where fluid regions were defined, it may be possible account for these local hot or cold spots. Despite the larger inaccuracies in level 7 of the HTP data comparison, most simulated data fit within the instrument tolerance.

The objective of this thesis was to assess the heat loss in the CNV using CFD simulations. The most important simulated data other than HTP wall temperatures used for the data comparison is the heat flux on the outer insulation wall. By generating data on the outer wall heat flux, the amount of heat that left via ambient convection can be estimated. Based on the maximum heat flux and the total outer surface area of the insulation allotted in the STAR CCM+ geometric model, the maximum heat loss for that moment can be calculated (units of Watts is Joules per second). The ratio of heat loss compared to the total power of the heater rods at the moment of the test came up to be 1.526%. It must be noted that out of all the transient experimental data collected from HP-16b, only the first pressurization was simulated. As part of setting boundary conditions, all wall thermal boundary conditions must be defined before the simulation can be started. Although on the CNV side known temperatures were able to be imported and the outer insulation wall can be set for environmental convection, the inner insulation wall temperatures cannot be known. To accommodate, the initial temperature was assumed to be pre-heated temperatures defined in section 5 in the enumerated procedure since by this point, steam has not been injected in the CNV yet. If simulations for latter pressurizations, the insulation temperatures would be truly unknown and unable to set initial boundary conditions. The initial boundaries would then be fed from the end of the first pressurization which has to be yet to be validated. Thus the maximum heat flux relative ratio is the lowest local maxima compared to pressurizations requiring higher pressures. A non-published previous study done by the author revealed that at power levels approximately four times higher than HP-16b, at least more than 0.256% (up to 0.769%) of the heat can be trapped in the CNV walls during an un-insulated HTP using two dimension steady state simulations. Therefore the outcome of this three dimension transient solution with the HTP insulated can be considered acceptable since the heat accumulated in the CNV walls would be greater giving a heat loss ratio at the insulation to be moderately higher than the heat accumulation of the CNV wall when the HTP is

not insulated. The heat loss of 1.526% of total power is small and can be negligible if it is within the tolerance of the NuScale Power hydraulic codes.

Future work on this topic would be to determine the original two-phase (three phase considering noncondensable air) flow simulation with the solid simulated in this thesis. With the injection system, turbulence model, condensation, pressure buildup, and heat transfer validation done, the maximum heat can be compared with data simulated in this thesis.

Bibliography

[1] United States Nuclear Regulatory Commision (U.S.NRC). Design certification application - nuscale. *U.S.NRC Website*, pages https://www.nrc.gov/reactors/new–reactors/design–cert/nuscale.html, 2012.

[2] V. Ciocan M. Verdes M.C. Balan A.A. Serbanoiu A. Burlacu, C.D. Lazarescu. Cfd heat transfer analysis for heat pipes integration into buildings with glazed facades. *Procedia Engineering*, 2016.

[3] M. Hamidi K. Farahmand, R. Srinivasa. Cfd heat transfer simulation of the human upper respiratory tract for oronasal breathing condition. *International Journal of Industrial Engineering Computations*, 2011.

[4] S.C. Vicent M. Bottcher R. Stieglitz J.P. Mañes, V.H.S. Espinoza. Validation of neptune-cfd two-phase flow models using experimental data. *Hindawi Publishing Corporation*, 2014.

[5] Y. Park K. Kang B. Yun B. Bae, S. Kim. Experimental investigation into the effect of the passive condensation cooling tank water level in the thermal performance of the passive auxiliary feedwater system. *Nuclear Technology*, 181:479–492, 2013.

[6] J.J. Utberg. Osu maslwr facility description report. *NIST-1*, 2016.

[7] J.J. Utberg. Nist-1 facility description report. *NIST-1*, 2017.

[8] CD-adapco. *USER GUIDE STAR-CCM+ Version 9.04*, 2014.

[9] V.P. Carey. *Liquid-Vapor Phase-Change Phenomena 2nd Edition*. 2008.

[10] J.J. Utberg. Hp-16b cnv heat loss test procedure. *NIST-1*, 2016.

[11] J.J. Utberg. Hp-16b cnv heat loss test report. *NIST-1*, 2017.

[12] United States Nuclear Regulatory Commision (U.S.NRC). Part 52 - licenses, certifications, and approvals for nuclear power plants. *U.S.NRC Website*, pages https://www.nrc.gov/reading–rm/doc–collections/cfr/part052, 2007.

[13] United States Nuclear Regulatory Commision (U.S.NRC). 50.33 contents of applications; general information. *U.S.NRC Website*, pages https://www.nrc.gov/reading–rm/doc–collections/cfr/part050/part050–0033.html, 2015.

[14] Siemens. Star-ccm+ discover better designs faster. 2016.

[15] L. Collins R. Bhaskaran. Introduction to cfd basics. *School of Mechanical and Aerospace, Cornell University*.

[16] et al. Shannon M. Bragg-Sitton. Star-ccm+ engineering disciplines. *CD-adapco*, 2016.

[17] M. Boucker P. Bouldier P. Fillion M. Grandotto J. Hérard E. Hervieu P. Péturaud A. Guilfi, D. Bestion. Neptune: A new software platform for advanced nuclear thermal hydraulics. *Nuclear Science and Engineering*, 156:281–324, 2007.

[18] P. Hao X. Fu, Z. Yao. Numerical simulation of condensation on structured surfaces. *Langmuir*, 30:14048–14055, 2014.

[19] C.W. Shin H.C. No B.G. Jeon, D.Y. Kim. Parametric experiments and cfd analysis on condensation heat transfer performance of externally condensing tubes. *Nuclear Engineering and Design*, 293:447–457, 2015.

[20] E.N. Wang N. Miljkovic, R. Enright. Effect of droplet morphology on growth dynamics and heat transfer during condensation on superhydrophobic nanostructured surfaces. *ACS Nano*, 6:1776–1785, 2012.

[21] M. McCarthy M. Rahman. Boiling enhancement on nanostructured surfaces with engineered variations in wettability and thermal conductivity. *Heat Trasnfer Engineering*, 38:1285–1295, 2017.

[22] F. Shi L. Yu X. Huang S. Hu B.Chen S. Ran S. Liu J. Liu, C. Fan. Fabrication of $cs_{0.32}wo_3/sio_2$ aerogel multilayer composite coating for thermal insulation applications. *Materials Letter*, 181:140–143, 2016.

[23] B. Sunden G. Xie T. Ji, R. Zhang. Investigation on thermal performance of high temperature multilayer insulations for hypersonic vehicles under aerodynamic heating conditions. *Applied Thermal Engineering*, 70:957–965, 2014.

[24] A. Pramuanjaroenkij S. Kakac, Y. Yener. *Convective Heat Transfer 3rd ed.* 2014.

[25] A. Eucken. Energie- und stoffaustausch an grenzflauchen. *Naturwissenschaften*, 25:209–218, 1937.

[26] M. Jakob. Heat transfer in evaporation and condensation. *Mech. Engrg.*, 58:643–660, 1936.

[27] P.J. Roache C.J. Freitas I.B. Celik, U. Ghia. Procedure for estimation and reporting of uncertainty due to discretization in cfd applications. *Journal of Fluids Engineering*.

APPENDICES

Appendix A: Operators

∇	Gradient
∇^2	Laplacian